A Coreflood-on-a-Chip Study of Viscoelasticity's Effect on Reducing Residual Saturation in Porous Media

Article *in* Water Resources Research · August 2021

DOI: 10.1029/2021WR029688

CITATION
1

READS
151

4 authors, including:

Yujing Du
Harvard University
8 PUBLICATIONS **102** CITATIONS
SEE PROFILE

Ke Xu
Peking University
39 PUBLICATIONS **744** CITATIONS
SEE PROFILE

Lucas Mejia
University of Texas at Austin
10 PUBLICATIONS **89** CITATIONS
SEE PROFILE

AGU ADVANCING EARTH AND SPACE SCIENCE

Water Resources Research

RESEARCH ARTICLE
10.1029/2021WR029688

A Coreflood-on-a-Chip Study of Viscoelasticity's Effect on Reducing Residual Saturation in Porous Media

Yujing Du[1], Ke Xu[2], Lucas Mejia[1], and Matthew Balhoff[1]

[1]Hildebrand Department of Petroleum and Geosystems Engineering and the Center for Subsurface Energy and the Environment, The University of Texas at Austin, Austin, TX, USA, [2]Department of Energy and Resources Engineering, Peking University, Beijing, China

Key Points:

- Viscoelasticity helps in reducing the residual fluid saturation without posing extraordinal large viscous force
- The residual saturation reduction attributes to viscoelastic instabilities induced reconnection and redistribution of residual ganglia
- Low salinity enhances the residual fluid reconnection and redistribution by swelling residual ganglia when elasticity is high

Supporting Information:

Supporting Information may be found in the online version of this article.

Correspondence to:

Y. Du,
yujingdu@utexas.edu

Citation:

Du, Y., Xu, K., Mejia, L., & Balhoff, M. (2021). A coreflood-on-a-chip study of viscoelasticity's effect on reducing residual saturation in porous media. *Water Resources Research*, *57*, e2021WR029688. https://doi.org/10.1029/2021WR029688

Received 24 JAN 2021
Accepted 4 JUL 2021

Abstract Polymer aqueous solutions are widely used in nonaqueous phase liquid recovery and aquifer remediation processes due to their high viscosity. Additional reduction of residual saturation by polymer's viscoelasticity has recently been discovered which elevates the ultimate displacement efficiency. However, there is no consensus on how, and under what conditions, viscoelasticity reduces residual saturation. This is in part because most studies utilize relatively low salinity and high viscosity, which also contribute to higher recoveries. We separate the effects of viscosity, elasticity and salinity, by performing microfluidic experiments in long (30 cm) heterogeneous glass micromodels (*coreflood-on-a-chip*). In the experiments, a highly viscous Newtonian aqueous phase flood is first performed so that the system reaches residual saturation, followed by polymer flood with varying elasticity and salinity. This is followed by another highly viscous Newtonian aqueous phase flood. We observe significant redistribution and reconnection of residual ganglia due to viscoelasticity induced instabilities during high-viscoelasticity polymer floods, which results in residual ganglia remobilization that ultimately reduces residual saturation. In contrast, no fluid redistribution and saturation reduction are observed in low-viscoelasticity polymer floods. During low salinity polymer floods (regardless of the relative elasticity), spontaneous emulsification occurs inside ganglia and results in ganglia swelling, which enhances ganglia reconnection when elastic instability happens, therefore amplifies the residual saturation reduction.

1. Introduction

Mechanistic description of capillary-trapped residual fluid behaviors during multiphase flow are crucial in many subsurface operations. Presence of nonaqueous phase liquids (NAPLs) in geologic porous media is ubiquitous. They can exist in the form of hydrocarbons, which are present both indigenously in hydrocarbon reservoirs and as transferable contaminants due to natural or human activities (e.g., oil spills; Geller & Hunt, 1993; Imhoff et al., 2002). The study of the displacement of NAPLs in porous media by fluid injection dates back to decades ago (Imhoff et al., 1994; Soerens et al., 1998), and evolves in different directions – environmental remediation (Ghosh et al., 2019; Philippe et al., 2020), hazardous waste disposal (Frollini et al., 2016), CO_2 geological sequestration (Hu et al., 2017; S. Wang et al., 2016), and hydrocarbon recovery (Farajzadeh et al., 2015; Jin et al., 2007; Mehmani et al., 2019). In all applications, residual fluid saturation and distribution pattern are important parameters in multiphase flow models. Experimental evidence of the residual fluid behaviors can therefore benefit general studies of fluid transport (e.g., NAPL recovery and remediation) in water contained porous media.

Normally, mobilizing and recovering capillary-trapped residual fluids is extremely challenging in geologic formations due to high capillarity ($Ca = \mu_i u/\gamma < 10^{-4}$) and low inertia ($Re = \rho u D/\mu_i << 1$). It is believed that capillary-trapped residual fluids cannot be recovered without posing large viscous forces (at high Ca). However, this theory is challenged when the displacing fluid is viscoelastic ($De = \tau_r \dot{r} > 1$). Viscoelastic fluids (e.g., many polymer aqueous solutions) are non-Newtonian fluids that exhibit both elastic (solid-like) and viscous (liquid-like) characteristics in response to mechanical deformation (Chen et al., 2010). They are commonly used in geological engineering processes such as enhanced oil recovery and groundwater remediation (Browne et al., 2020b; Lake et al., 2014; Sorbie, 1991). Traditional theories assume that the improved displacement efficiency by polymer injection is due to the high viscosity and sweep efficiency improvement, but capillary-trapped residual hydrocarbon saturation should not change (Delshad et al., 2008; Hirasaki & Pope, 1974; Lake et al., 2014; Sorbie, 1991). However, many recent experimental studies have reported

reduction of capillary-trapped, residual fluid saturation after high-viscoelasticity polymer flood, though the saturation reduction varies without consensus of its mechanisms (Erincik et al., 2018; Jin et al., 2020; Vermolen et al., 2014; D. Wang et al., 2000, 2001; Xia et el., 2004, 2007).

Macroscopic investigation of coreflood in rocks have demonstrated that the residual oil saturation after well-performed secondary waterfloods (or other inelastic aqueous phase floods) can be further reduced by the injection of high-viscoelasticity polymer solutions (Erincik et al., 2018; Jin et al., 2020; Qi et al., 2017; Vermolen et al., 2014). Surprisingly, residual oil reduction was observed not only during the high-viscoelasticity polymer flood, but also in a follow-up flood with low-viscoelasticity fluids (Erincik et al., 2018; Jin et al., 2020). Despite these and other positive results mentioned in the literature, other studies reported no, or very little, residual oil recovery from high-viscoelasticity polymer floods in tertiary floods (Huh & Pope, 2008; Sandengen et al., 2017). The inconsistences in literature are not well explained by established theories or experimental evidences retrieved from core-scale.

Viscoelastic flows exhibit nonlinear instabilities that lead to flow turbulence even at low inertia scenarios (Groisman & Steinberg, 2000; Ho & Denn, 1977; Morozov & van Saarloos, 2007), which has been hypothesized as a cause of the observed saturation reduction in porous media. Microfluidic studies have captured the occurrence of viscoelastic instabilities at the pore-scale during viscoelastic polymer floods. Periodic oil droplet oscillation was observed when oil was displaced by viscoelastic polymer solutions in a contraction-expansion single channel geometry, which was hypothesized to contribute to residual oil saturation reduction (Qi, 2018). Pore-scale, lattice Boltzmann simulations also showed that residual droplets can be oscillating as the flow streamlines become chaotic and form vortices that may finally recover the droplet (Xie et al., 2020). Residual ganglia fluctuation and mobilization caused by viscoelastic displacing fluids were observed in micromodels with a two-dimensional (2D) pore-network (Clarke et al., 2016; Mitchell et al., 2016). However, despite these pore-scale viscoelastic instabilities, direct recovery of individual residual droplets by oscillation and fluctuation are observed only at large viscous forces that are rarely encountered in subsurface porous media.

Direct pore-scale visualization at high time resolution with realistic porous structures is required to experimentally reveal viscoelasticity's role in reducing residual fluid saturation. Visualization of corefloods in rocks is challenging. Micro-computed tomography technology is an emerging method to visualize rocks (Blunt et al., 2013; Gao et al., 2017; Wildenschild & Sheppard, 2013), but the time resolution is restricted, and the sample sizes are usually limited. In addition, three-dimensional (3D) imaging/analysis of ganglia in porous media is possible with magnetic resonance imaging for finer effective resolution (Johns and Gladden, 2000, 2001). Microfluidics is a fast screening tool for investigating flow dynamics at the pore-scale and even representative elementary volume scale (Anbari et al., 2018; Lifton, 2016; Mehmani et al., 2020). It is commonly used to study multiphase flow processes encountered in subsurface environments, such as NAPL displacement (de Castro et al., 2015; Phenrat et al., 2011; Zhong and Mayer, 2001) and hydrocarbon recovery (Du et al., 2020; Li et al., 2020; Mejia et al., 2019; Yun et al., 2020).

In this study, we revealed the fundamental details of the residual fluid reduction during a particular multiphase flow under generic geologic conditions at high viscoelasticity ($De > 1$), low inertia ($Re << 1$) and high capillarity ($Ca < 10^{-4}$). We performed systematic experiments utilizing a long (30 cm), heterogeneous two and half dimensional (2.5D) glass micromodel (*coreflood-on-a-chip*). Direct visualization at the REV scale and the pore-scale are obtained and analyzed. Through the observations and analysis, we are able to analyze the behaviors of the residual ganglia and demonstrate a correlation between flood viscoelasticity and the residual saturation reduction in complex porous media. We, therefore, present an advancement in investigating new mechanisms for the multiphase flow in geologic porous media.

2. Materials and Methods

2.1. Materials and Fluids

Experiments were performed in a 30-cm long, 2.5D, water-wet glass micromodel with heterogeneous porous matrix (*coreflood-on-a-chip*; Figure 1). A 2.5D micromodel is a type of micromodel that includes pore-scale 3D features in the traditional 2D design by having different etching depths at the pore bodies and the pore throats (Xu et al., 2017). The micromodel was designed and fabricated in house using the protocols

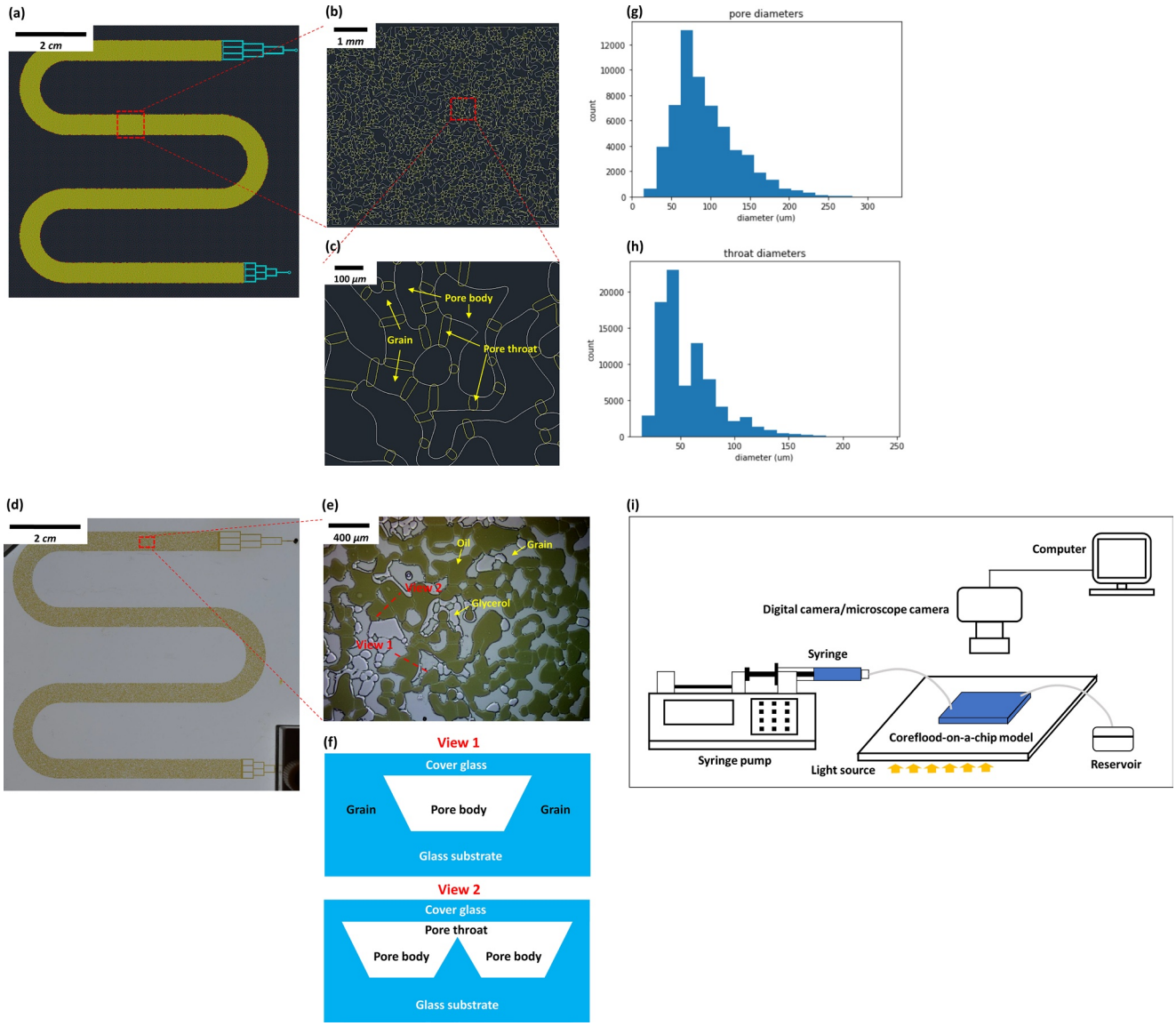

Figure 1. (a) Photomask design of the micromodel in AutoCAD. (b) A cross-section of the photomask design captured from image (a). (c) The pore body, pore throat and grain in the photomask design. (d) Image of the micromodel M2 saturated with crude oil (brown) captured by a digital single-lens reflex (DSLR) camera. (e) Microscopic image of pores with crude oil (brown) and glycerol (white) from another case than (d). Two cross-sections at view 1 and view 2 are demonstrated in planar view. (f) Cross-sectional schematics of the micromodel pore body/grains at view 1 and pore bodies/pore throat at view 2. (g) The distribution of the radial pore diameter (averaged 95 μm) in the pore-network. (h) The distribution of the radial pore throat (averaged 57 μm) in the pore-network. (i) Schematic sketch of the experimental setup.

described in previous works (Mejia et al., 2020). The patterns of the micromodel were designed in a computer-aided design software and were then used to generate a photomask for photolithography. Photolithography and wet-etching using hydrofluoric acid were conducted to engrave the designed patterns onto the glass substrate. Holes were drilled through the substrate glass at both ends of the geometry as the inlet and the outlet. Soda-lime glass (2 mm thick) was used for both substrate and cover glass. The etched and drilled substrate glass and the smooth cover glass were subsequently bonded together using the thermal bonding method. The micromodel was designed to be serpentine-shaped (Figures 1a and 1d) to reduce the overall size considering space limitations.

The novel *coreflood-on-a-chip* model better mimics real rocks than many other micromodels while maintaining the advantageous features of traditional microfluidics. Pore-scale 3D (or 2.5D) features are

Table 1
Micromodel Properties

	Length	Width	Pore body depth	Pore throat depth	Porosity	Pore volume
M1	30 cm	5.6 mm	15.5 μm	6 ± 1 μm	0.60	15.9 μl
M2	30 cm	5.6 mm	15.0 μm	6 ± 1 μm	0.55	14.1 μl

achieved by etching the pore throats shallower than the pore bodies (Figures 1e and 1f) so that the grains are also connected, allowing the occurrence of Roof capillary snap-off (Xu et al., 2017). Roof capillary snap-off refers to the capillary snap-off of the non-wetting phase at the pore-neck or pore-throat locations due to the capillary pressure imbalance, which was first studied by Roof (1970). Heterogeneity is included in the pore-network (Figures 1b and 1c) which is an important feature that impacts the drainage dynamics and therefore the microscopic displacement. To generate the heterogeneous pore-network, a random set of points with a Gaussian kernel was convolved, then the surface produced by the convolution was thresholded to obtain the pore and grain spaces. The distributions of the radial pore diameter (averaged 95 μm) and the radial pore throat (averaged 57 μm) are shown in Figures 1g and 1h. See the supporting information Section S8 for more details regarding the fabrication procedure. The long length (30 cm) minimizes the potential scale issues in many micromodels, for example, capillary end effects, thus providing a more realistic experimental environment (Mejia et al., 2020). Two micromodels denoted as M1 and M2 with the same design and nearly identical geometric properties were used in this work. The permeability for the micromodels was 0.87 Darcy determined by Darcy's law by measuring pressure drops under constant injection rates (see the supporting information Section S9). The geometric properties of the micromodels are listed in Table 1.

A crude oil sample with a viscosity of 13 cp and a density of 0.8 g/cm^3 at room temperature was used in all 10 flow experiments (denoted as experiments 1–10) as the displaced phase. Two glycerol solutions (glycerin mixed with deionized water), were used in the experiments as the Newtonian non-polymer aqueous phases instead of water. The glycerol solutions were more viscous than the crude oil which can prevent the generation of viscous fingering caused by an unfavorable mobility ratio. Two viscosities were used to exclude potential impact of initial viscosity variation on the results. Viscosity of the two glycerol fluids were measured using ARES-G2 rotational rheometer. The properties of the two glycerol solutions at ambient conditions are listed in Table 2.

Table 2
Compositions and Properties of the Displacing Fluids

Displacing fluids	Glycerol solution1	Glycerol solution2	Elastic polymer1	Elastic polymer2	Inelastic polymer1	Inelastic polymer2
Content	Glycerol	Glycerol	HPAM (molecular weight of 18–20 million Daltons)	HPAM (molecular weight of 24–28 million Daltons)	HPAM (molecular weight of 18–20 million Daltons)	HPAM (molecular weight of 3–4 million Daltons)
Concentration	84 vol%	70 vol%	1,000 ppm	1,800 ppm	2,200 ppm	1,800 ppm
Salts	–	–	1,000 ppm NaCl, 400 ppm $NaHCO_3$	20,000 ppm NaCl, 400 ppm $NaHCO_3$	20,000 ppm NaCl, 400 ppm $NaHCO_3$	1,000 ppm NaCl
Relaxation time (τ_r)	–	–	1.49 s	1.34 s	0.048 s	0.013
Shear rate[a] ($\dot{\gamma}$)	–	–	122–132 s^{-1}	~122 s^{-1}	133–145 s^{-1}	159–163 s^{-1}
Apparent viscosity (μ)	118 cp	33 cp	12–13 cp	~16 cp	14–15 cp	14–15 cp
Deborah number (De)	–	–	182–196	163	6.4–7	~2
Density (ρ)	1.25 g/ml	1.20 g/ml	1.02 g/ml	1.04 g/ml	1.04 g/ml	1.02 g/ml
IFT[b] with crude oil (γ)	20.0 ± 0.3 mN/m	18.7 ± 0.5 mN/m	5.4 ± 0.6 mN/m	0.93 ± 0.06 mN/m	0.84 ± 0.006 mN/m	12.5 ± 0.2 mN/m

Abbreviations: HPAM, partially hydrolyzed polyacrylamide; IFT, interfacial tension.

[a]Some parameters used to determine shear rate were estimated according to consensually accepted empirical data in literature; variations in the reasonable range would not qualitatively affect the results presented in this study.

[b]IFT is short for interfacial tension; multiple measurements were conducted and averages values were reported.

Four polymer solutions prepared with three different molecular weight partially hydrolyzed polyacrylamide (HPAM) polymer powders (Table 2) were used in the experiments and denoted as "elastic polymer 1," "elastic polymer 2," "inelastic polymer 1," and "inelastic polymer 2," respectively. Deborah number (*De*) is a dimensionless number that describes the ratio of elastic to viscous forces. The viscoelastic effect was assumed to occur only when *De* is larger than 1 when the viscoelastic flow instabilities initiate (Larson, 1992), but higher values (>10) may be required in porous media to see significant saturation reduction (Erincik et al., 2018). The terms "elastic" and "inelastic" are relative, which refer to high-elasticity polymers ($De > 100$) and low-elasticity polymers ($De < 10$), respectively. Elastic polymer 1 and inelastic polymer 2 were at low salinity (1,000 ppm NaCl), and elastic polymer 2 and inelastic polymer 1 were at relatively high salinity (20,000 ppm NaCl). All polymer solutions were made significantly less viscous than the glycerol solutions at the experimental conditions (Figure 2a) so that any additional recovery was not due to sweep efficiency improvement by elevated viscosity. The rheology of the polymer solutions was measured using an ARES-G2 rotational rheometer, and the interfacial tensions (IFTs) between oil and the four displacing fluids were measured using a spinning drop tensiometer (KRÜSS SDT) at room temperature. The compositions and properties of the polymer solutions at experimental conditions are listed in Table 2.

The viscosity versus shear rate curves of the polymer solutions are shown in Figure 2. The polymer solutions have similar viscosity in a shear rate range of 10–300 s^{-1} which covers the approximate flow regimes in the experiments. Relaxation times of the polymer solutions were estimated as the inverse of angular frequency at the crossover point of storage (G') modulus and loss modulus (G'') which were measured from dynamic rheology tests (Castelletto et al., 2004; Qi et al., 2017; Vermolen et al., 2014; Volpert et al., 1998) as shown in Figures 2b, 2c, 2d and 2e. There are multiple methods used to determine the relaxation time of polymers (Clarke et al., 2016; Delshad et al., 2008; Mohagheghi & Khomami, 2016). In this study, we did not compare the relaxation time determined using different methods. The values obtained from the crossover of the G' and G'' has been a straightforward approach to estimate the elasticity of polymer solutions (Erincik et al., 2018; Sheng, 2010; Volpert et al., 1998). The relaxation time of the elastic polymer solutions (1.49 and 1.34 s) is one to two orders of magnitude higher than the two inelastic polymers solutions (0.048 and 0.013 s), indicating much higher elasticity in the former two polymers. The method used to determine polymers' rheological properties listed in Table 2 is explained in Appendix A.

2.2. Experiments

Ten flow experiments were conducted in the *coreflood-on-a-chip* micromodel at ambient conditions on the experimental platform illustrated in Figure 1i. Experiments 1–8 were visualized at the macroscale, and experiments 9 and 10 were visualized at the microscale. In each experiment, an initial condition with oil and residual aqueous fluid was established by a primary oil flood into the micromodel saturated with viscous Newtonian aqueous fluids to mimic the subsurface environment. After establishing the initial condition, three floods were performed in order. The first, second, and third flood are termed as secondary, tertiary, and post-tertiary flood, respectively, in this study. The secondary flood used a highly viscous Newtonian aqueous fluid to achieve the residual saturation of oil, and to exclude the effect of viscosity on residual saturation reduction in following floods. The tertiary flood used polymers with different elasticity and salinity to explore the effects of these factors. The post-tertiary flood used the same fluid as in the secondary flood to determine the potential longer-term impacts of the tertiary flood. Table 3 summarizes the saturating fluids and displacing fluids used in each experiment.

In experiments 1–8, the micromodel was placed on top of a white light emitting diode (LED) light pad, and a digital single-lens reflex (DSLR) camera (Nikon D5600) was mounted above the micromodel using a tripod stand to capture time-lapse images of the entire flow geometry. The image dimensions are 6,000 × 4,000 pixels with voxel resolution of approximately 20 micrometers/pixel. The exposure time was constant for each experiment (1/250 s in experiments 1–3, and 5, and 1/200 s in experiments 4 and 6–8). Experiments 9 and 10 were conducted under a microscope (AmScope IN300TC), where pore-scale images of a fixed area of 2 × 2.6 mm were captured by the microscope camera (AmScope 10MP) mounted above the micromodel. The image dimensions are 3,584 × 2,748 pixels with voxel resolution of 0.8 micrometers/pixel. The exposure time was fixed once an optimal exposure was achieved before each experiment. The exposure time was 1/23 and 1/30 s for experiments 9 and 10, respectively.

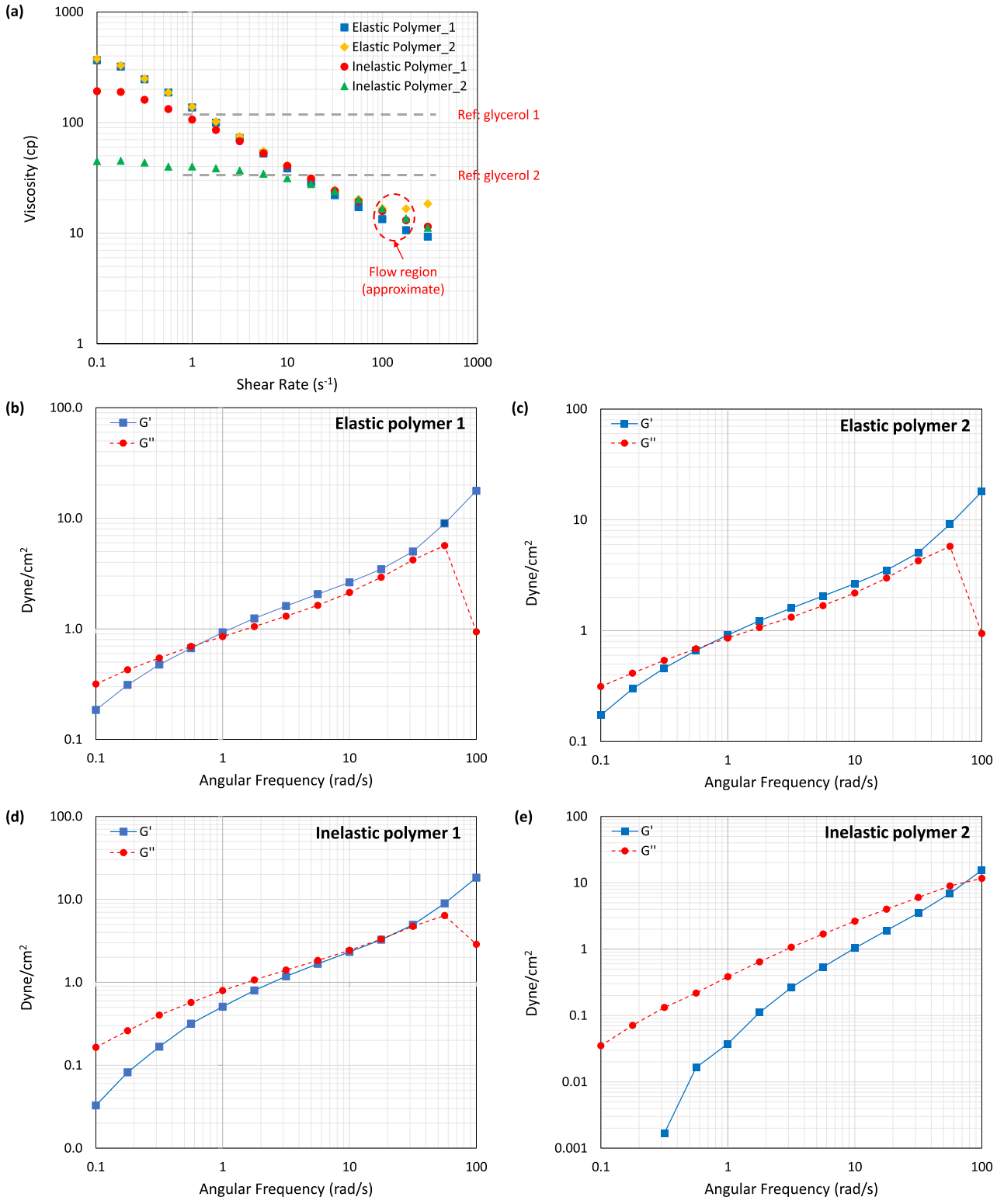

Figure 2. (a) Rheological behaviors of partially hydrolyzed polyacrylamide (HPAM) polymers solutions denoted as elastic polymer, inelastic polymer 1 and inelastic polymer 2. G'/G'' plots of (b) elastic polymer 1, (c) elastic polymer 2, (d) inelastic polymer 1, and (e) inelastic polymer 2.

Water Resources Research

10.1029/2021WR029688

Table 3
Fluids and Volumes Used in Each Flood in Experiments 1–10

Experiment	1	2	3	4	5	6	7	8	9	10
Elasticity[a] of 2nd flood	High	High	High	High	Low	Low	Low	Low	High	High
Salinity[b] of 2nd flood	Low	Low	Low	High	High	High	Low	Low	Low	Low
Initial saturating fluid	Glycerol1	Glycerol1	Glycerol2	Glycerol1	Glycerol1	Glycerol2	Glycerol2	Glycerol1	Glycerol1	Glycerol2
1st flood fluid type	Glycerol1	Glycerol1	Glycerol2	Glycerol1	Glycerol1	Glycerol2	Glycerol2	Glycerol1	Glycerol1	Glycerol2
2nd flood fluid type	Elastic polymer1	Elastic polymer1	Elastic polymer1	Elastic polymer2	Inelastic polymer1	Inelastic polymer1	Inelastic polymer2	Inelastic polymer2	Elastic polymer1	Elastic polymer1
3rd flood fluid type	Glycerol1	Glycerol1	Glycerol2	Glycerol1	Glycerol1	Glycerol2	Glycerol2	Glycerol1	Glycerol1	Glycerol2
1st flood pore volumes	6.7	3	4.5	4.3	3	3.5	2.6	3.2	2	2
2nd flood pore volumes	5	6	6.2	7.9	8	8.7	8.7	8.7	7.4	7.5
3rd flood pore volumes	2.3	3.6	3	3.5	3	3.5	3.5	3.5	2.3	2.5
Micromodel #	M1	M1	M1	M2	M1	M2	M2	M2	M1	M1

Experiments 1–8 were visualized at the macroscale, and experiments 9 and 10 were visualized at the microscale.
[a]The high and low elasticity refer to $De > 100$ and $De < 10$, respectively, using the definition in this work.
[b]The high and low salinity refer to 20,000 and 1,000 ppm NaCl, respectively.

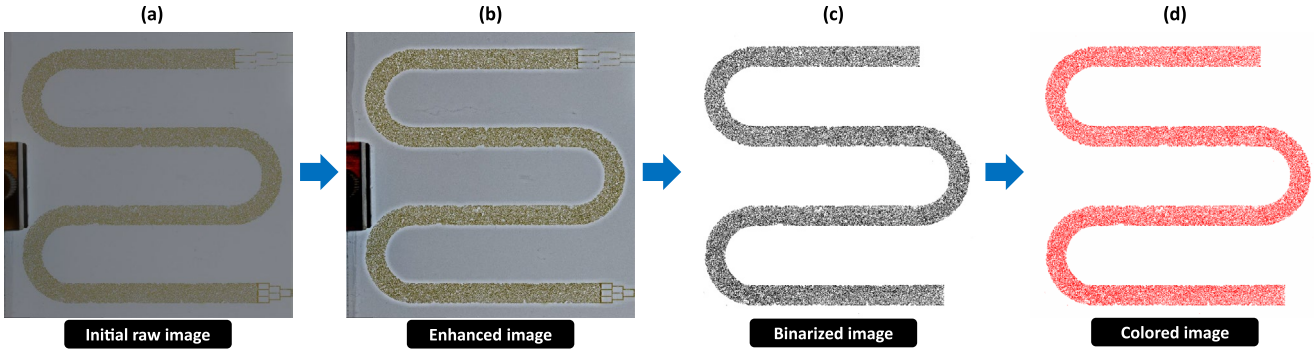

Figure 3. Image processing procedures. Oil phase is in brown in (a) and (b). (c) Gray scale image in black (oil) and white. (d) Image with adjusted color in red (oil) and white.

When performing the experiments, the micromodel was first saturated with the saturating fluids (glycerol solutions) by injecting at about 50 μl/h from the inlet for sufficient time (>24 h) using a syringe pump (PHD 2000; Harvard Apparatus). If necessary, another syringe was used to vacuum from the outlet until gas bubbles disappeared from the system. After the saturation, oil was injected at 20 μl/h until no more existing aqueous phase was produced and a steady state was reached. The subsequent three floods were performed in order at an injection rate of 1.65 μl/h (~1.5 ft/day). The capillary numbers ($Ca = \mu_i u/\gamma$) of the floods by the four displacing fluids were in the range of 6×10^{-6}–9×10^{-5}, therefore, capillary desaturation was minimal and residual oil saturation was not affected by varying capillary number (Lake et al., 2014; Qi et al., 2017). The Reynold number (Re) in the experiments are much less than 1, $\sim 10^{-6}$, and its variation has minimal impact on the flow dynamics. After each experiment, the micromodel was cleaned by injecting solvents (hexanes and acetone) and deionized water in order, and ultrasonic cleaner (Branson 2800) was also used to help clean solid debris on the surface. After cleaning, the micromodels were dried on a hot plate at 110°C.

2.3. Image Processing

An open sourced software, ImageJ, was used to process the images and the processing procedures were demonstrated in Figure 3. A series of images captured in one experiment were imported into ImageJ as an image stack, then registration was applied to the stack of images using "Linear Stack Alignment" function to align all images to the same position. Images were cropped around the geometry of interest subsequently and then enhanced using "Enhanced Local Contrast (CLAHE)" function to improve the contrast and to make phase boundaries clearer (Figure 3b). The enhanced images were then binarized into black (oil) and white colors (the other fluid and grains) using thresholding method "Otsu" function (Figure 3c). Oil saturation was calculated from the binarized images by dividing the fraction of the black area in each image to the fraction of the black area. Colors were added to binarized gray scale images in some cases by adjusting the Look-Up Table (LUT for color mapping) to the index value of the color (Figure 3d).

3. Results

3.1. Qualitative Results

Figure 4 shows the oil distribution initially (Figure 4a) and at the end of secondary (Figure 4b), tertiary (Figure 4c) and post-tertiary floods (Figure 4d) in experiments 1–8. The images in each column are from the same experiment. Zoomed-in images from experiments 1 and 4 after secondary, tertiary, and post-tertiary floods are presented in Figure 4e for detailed observation. Experiments 1–4 are high elasticity and experiments 5–8 are low elasticity; experiments 1–3 and 7–8 are low salinity and experiment 4–6 are high salinity. No unswept regions or fingering were observed in all experiments, since the invading fluids used in secondary floods are much more viscous than the defending fluid (oil). In all experiments, the displacement fronts in the secondary flood were stable, and the entire porous medium behind the fronts was swept by the invading glycerol solutions, as seen from the zoomed-in images in the supporting information Figure S1.

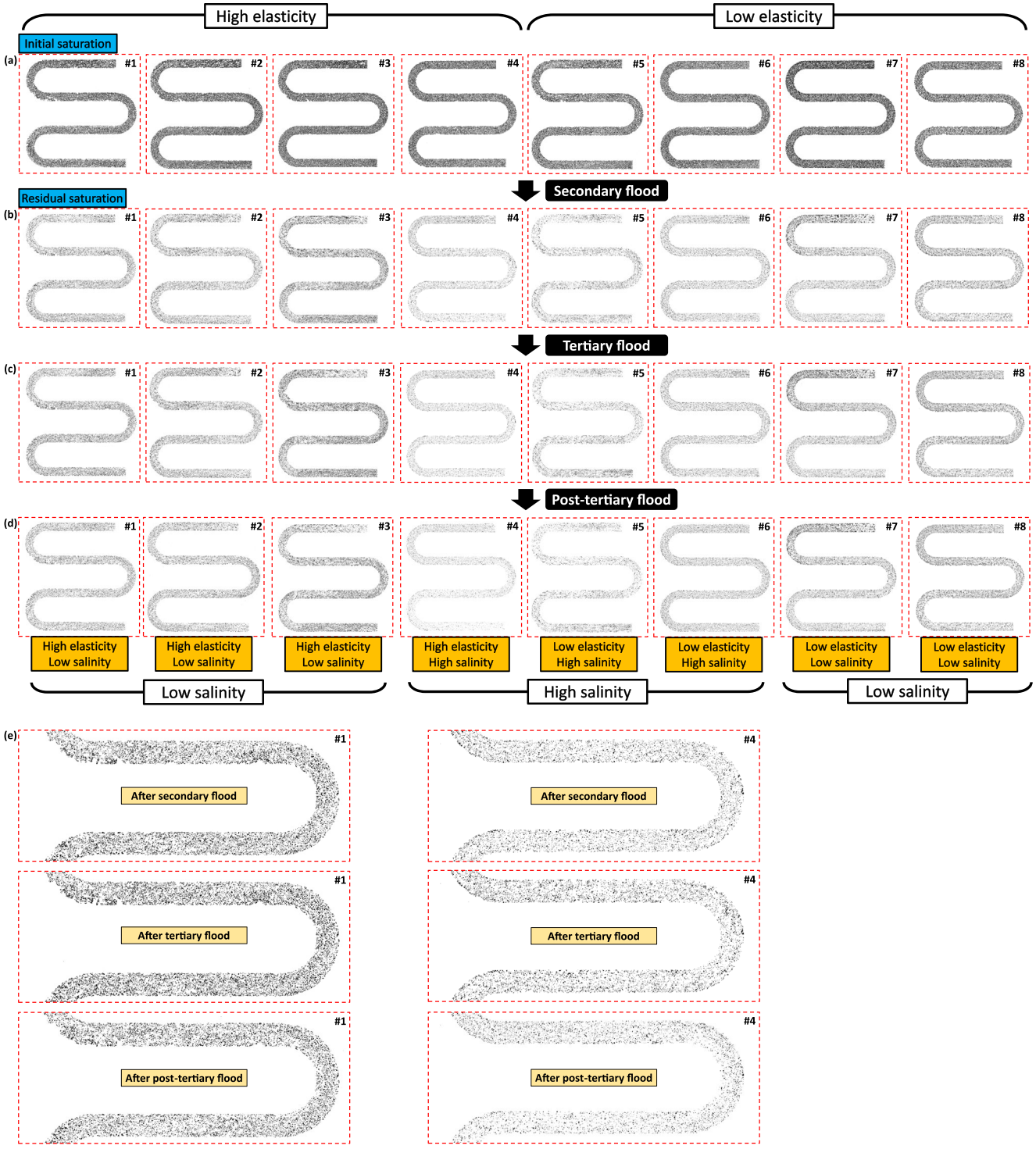

Figure 4. Oil (black) distribution in the micromodel at (a) initial oil saturation, (b) residual oil saturation at the end of secondary flood, (c) end of tertiary polymer flood, and (d) end of post-tertiary flood. (e) Zoomed-in images in the middle of the *coreflood-on-a-chip* geometry from Experiment 1 (low salinity, high elasticity) and Experiment 4 (high salinity, high elasticity) after the secondary, tertiary, and post-tertiary floods, respectively. Experiment number (#) is labeled at the top right corner in each image.

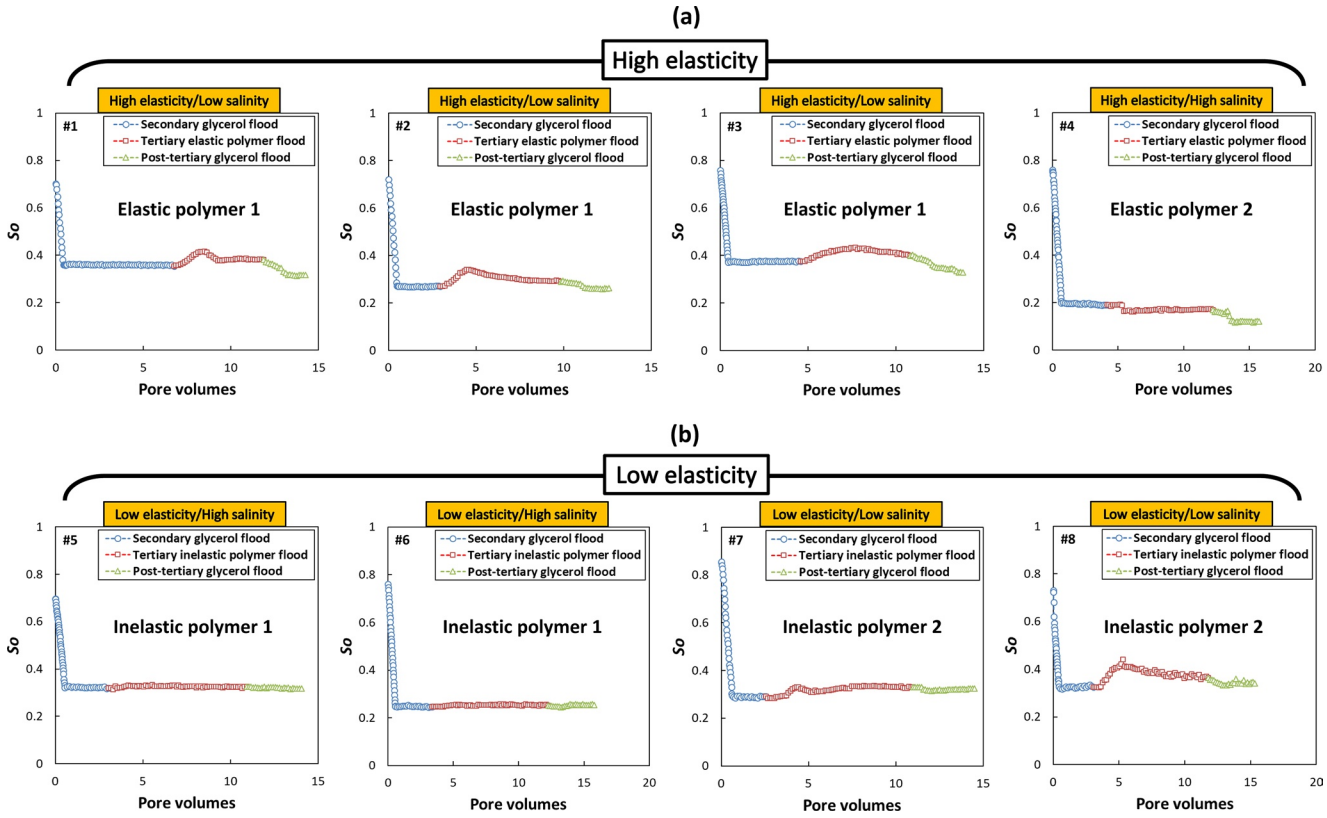

Figure 5. Oil saturation curves in each experiment for experiments 1–8 with (a) high elasticity in tertiary flood and (b) low elasticity in tertiary flood. Experiment number (#) is labeled at the top left corner in each image.

This is consistent with the favorable mobility ratio between the displacing phase (glycerol solution) and the displaced phase (oil). We, therefore, ensure that the remaining defending fluid is at residual saturation. See more details in the supporting information Section S1.

3.2. Quantitative Results

Oil saturations from the binarized images are quantitatively analyzed by the image analysis software (ImageJ). Oil saturation versus injected pore volumes in experiments 1–8 are shown in separate plots numbered #1–#8 in Figure 5, with high-elasticity cases (#1–#4) in Figure 5a and low-elasticity cases (#5–#8) in Figure 5b. The saturation and changes are also summarized in Table 4. The variation in the initial and residual oil saturations in parallel experiments 1–8 were largely due to technical reasons, and does not compromise the reproducibility and conclusions of this work (see the supporting information Section S2). In each plot in Figure 5, there are three stages marked with three colors (blue, red, and green), representing the secondary, tertiary, and post-tertiary floods, respectively.

Residual saturation after secondary aqueous flood: Secondary flood decreases the oil saturation from the initial saturation of 70%–85% to the residual saturation of 19%–37%, where a plateau is reached with additional pore volumes injected in each of the eight experiments.

Saturation increase in tertiary polymer flood: Unexpected *saturation increase* is observed during tertiary polymer flood in all cases that the polymer salinity is low (#1–#3, #7, and #8). In plots #1–#3, the saturation increases during the first several pore volumes of injection and then decreases, but is still higher by 2.0%–2.7% at the end of the tertiary floods than before them. In plots #7 and #8, similar to the trend in #1–#3, the saturation increases and then decreases with an increase of 3.8% and 4.0%, respectively, at the end of the tertiary floods. In plot #4, the saturation decreases by 2% and no saturation increase is observed at any point during the flood. In plots #5 and #6, the saturation curves remain flat during the entire flood.

Table 4
Oil Saturation and Changes in Each Flood in Experiments 1–8

Experiment	1	2	3	4	5	6	7	8
Elasticity of 2nd flood	Elastic polymer 1	Elastic polymer 1	Elastic polymer 1	Elastic polymer 2	Inelastic polymer 1	Inelastic polymer 1	Inelastic polymer 2	Inelastic polymer 2
Salinity of 2nd flood	High	High	High	High	Low	Low	Low	Low
Salinity	Low	Low	Low	High	High	High	Low	Low
Soi	0.70	0.72	0.76	0.76	0.70	0.76	0.85	0.73
So after 1st flood	0.357	0.270	0.375	0.19	0.23	0.25	0.290	0.327
Δ*So* in 1st flood	−0.343	−0.450	−0.375	−0.57	−0.47	−0.50	−0.560	−0.403
So after 2nd flood	0.381	0.290	0.400	0.17	0.23	0.25	0.330	0.365
Δ*So* in 2nd flood	+0.024	+0.020	+0.027	−0.02	0	0	+0.040	+0.038
So after 3rd flood	0.317	0.260	0.327	0.12	0.23	0.25	0.320	0.343
Δ*So* in 3rd flood	−0.064	−0.030	−0.073	−0.05	0	0	−0.008	−0.022
$\Delta So_{(net)}$ from 2nd and 3rd floods	−0.040	−0.010	−0.048	−0.07	0	0	+0.032	+0.017

Note. The saturation change at each step (Δ*So*) is calculated by subtracting the post-flood saturation by the pre-flood saturation.

Saturation reduction in post-tertiary aqueous flood: saturation reduction is obtained in several cases (#1–#4, #7, and #8) during the post-tertiary flood. In plots #1–#4, the oil saturation decreases by 3.0%–7.3% to the final saturation which is lower than the saturation at the end of the secondary flood. In plots #5 and #6, the curves remain almost flat during the entire flood. In plots #7 and #8, the saturation decreases by 0.9%–2.2% to the final saturation which is still higher than the saturations at the end of the secondary flood.

Despite of the saturation changes, oil was only produced in high-elasticity cases (#1–#4) during post-tertiary flood in #1–#3 and both tertiary and post-tertiary floods in #4, determined from the produced fluids. This observation and the *saturation increase* from the low-salinity tertiary flood are discussed in Section 4. Three cases were repeated (two to three times) and we were able to obtain the same qualitative results. Importantly, we repeatedly observed the residual saturation reduction in high-elasticity cases (experiments 1–4), which was not observed in low-elasticity cases (experiments 5–8).

Elasticity and salinity of the polymers are the two factors shown to affect the flow dynamics and the reduction of residual saturation. The key findings with regards to these two factors are subsequently summarized in Figure 6 schematically, and are discussed in Section 4. When the elasticity was high, residual ganglia recovery and ultimate residual saturation reduction were obtained. No recovery or residual saturation reduction was obtained when elasticity was low. Most of the recovery was obtained from post-tertiary inelasticity flood which was also observed in corefloods (Erincik et al., 2018; Jin et al., 2020). Oil *saturation increase* was observed when polymer salinity was low (1,000 ppm NaCl) regardless of elasticity, and was not observed when polymer salinity was relatively high (20,000 ppm NaCl).

4. Analysis and Discussion

4.1. Microscopic Observation

Unexpected oil *saturation increase* during low salinity tertiary polymer flood was observed in experiments 1–3, 7, and 8, despite the salinity of the previous flood (glycerol solutions) was also low. To explore the

(a)

Polymer elasticity	Polymer salinity	Polymer flood performance		Ultimate recovery
		Oil swelling (saturation increase)	Recovery	
High	Low	Yes	No	Yes
	High	No	Yes	Yes
Low	Low	Yes	No	No
	High	No	No	No

(b)

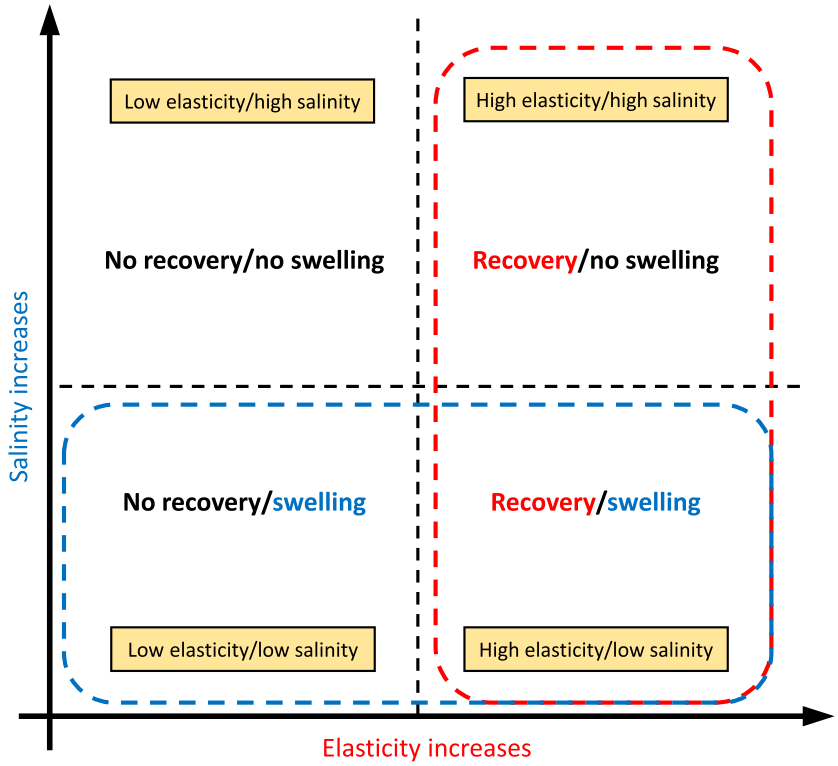

Figure 6. Schematic summary of the results presented in Sections 3.1 and 3.2. (a) Summary of behaviors using different polymer solutions. (b) Conceptual diagram based on polymer elasticity and salinity conditions.

underlying reason for the *saturation increase*, pore-scale observations were conducted in experiments 9 and 10 under a microscope using the fluids shown in Table 3. A fixed view of an area of 2 × 2.6 mm was captured during experiments and the visualizations are presented.

4.1.1. Residual Ganglia Swelling in Tertiary Polymer Flood

After the secondary flood, residual oil ganglia distributed in the captured area in the middle of individual pores or occupying multiple pores (left column of Figure 7a). Upon the start of the low salinity, high-elasticity polymer flood (elastic polymer 1), emulsions (dark phase within oil ganglia) began to form inside the oil ganglia (middle column of Figure 7a). The emulsions caused ganglia swelling that lead to the *saturation increase* and contributed to ganglia reconnection. The peak amount of emulsions occurred during the first several pore volumes of injection (middle column of Figure 7a), after which point emulsions began to subside and the oil ganglia partially de-swelled as a consequence. The observed non-monotonic oil swelling explains the oil saturation increase followed by decrease shown in Figure 5. In this process, some oil ganglia moved in the transverse direction but did not move out in the longitudinal direction. The transverse movement was not (at least not mainly) caused by low salinity induced swelling, although swelling assisted the movement (see the supporting information Section S3).

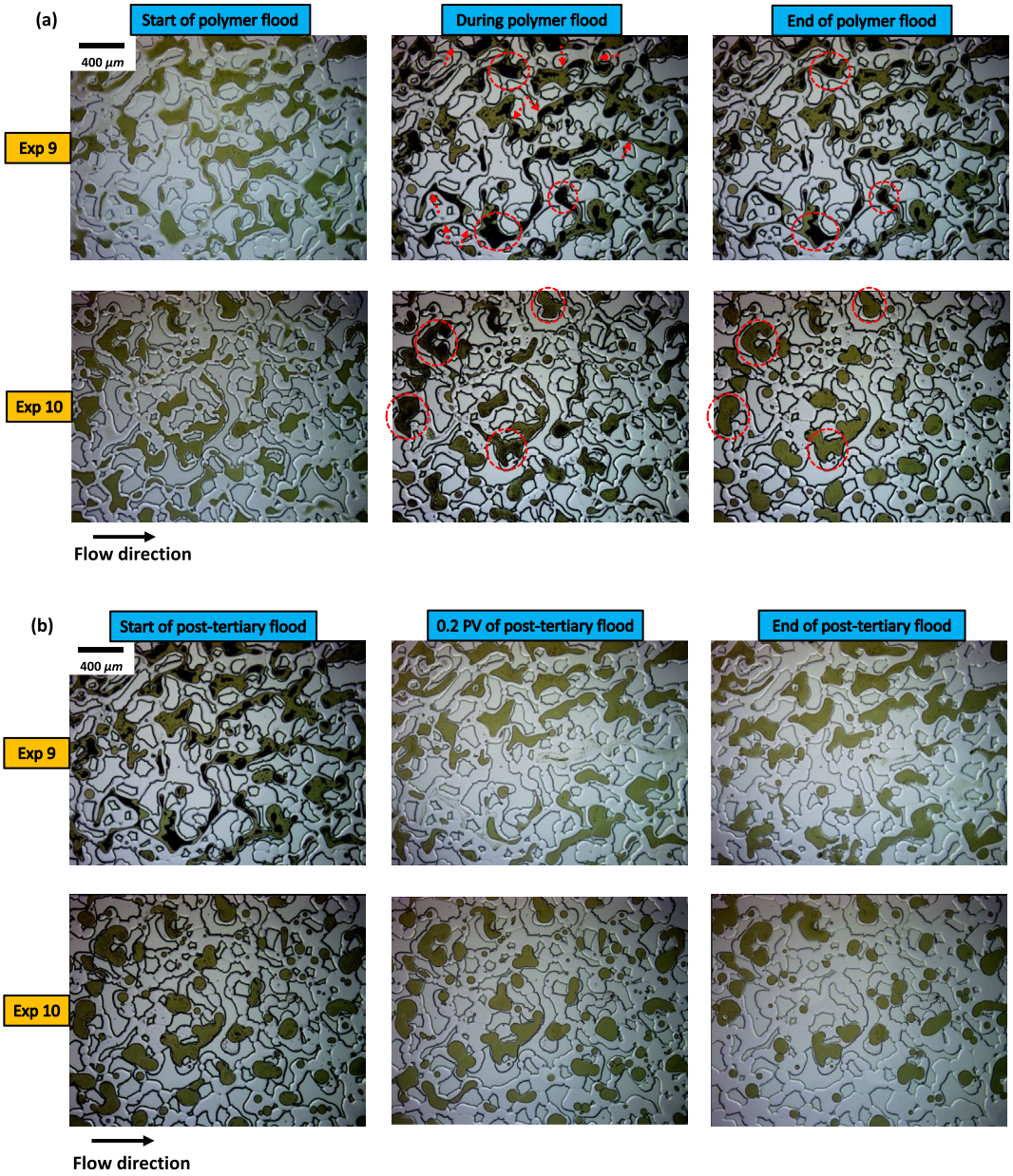

Figure 7. Pore-scale visualization of residual oil ganglia in experiments 9 (top row) and 10 (bottom row) during (a) tertiary polymer flood (high elasticity and low salinity), and (b) post-tertiary glycerol flood with oil (brownish) and glycerol (white). Red circles in (a) highlight the emulsifications (dark) inside the oil phase; red arrows in (a) point to locations where oil interfaces change and oil ganglia reconnect.

4.1.2. Residual Ganglia Mobilization in Post-Tertiary Aqueous Phase Flood

During the post-tertiary glycerol flood the emulsions quickly subsided and eventually almost disappeared after a short period of injection (0.1–0.2 pore volumes), despite the salinity of the glycerol solutions were also low. Meanwhile, the residual oil ganglia left behind in previous two floods became mobilized and flowed out of the observed area in the longitudinal direction. Ganglia de-swelling and break-up were also observed in the captured area (Figure 7b). The observation agreed with the macroscopic observation from experiments 1 to 3, and further confirmed that the decrease in saturation in the post-tertiary flood in these experiments were from oil mobilization in addition to de-swelling.

4.2. Ganglia Analysis in Single Cross-Sections

Low polymer salinity induced swelling explains the observed *saturation increase*, but does not have a determinant impact on the residual oil recovery (Figure 6). Instead, saturation reduction and residual oil recovery were obtained only when the tertiary flood had high elasticity as in experiments 1–4. To reveal the role of elasticity on saturation reduction and residual oil recovery, ganglia analysis in single cross-sections zoomed-in from the macroscopic visualizations was performed.

4.2.1. Residual Ganglia Swelling, Redistribution, and Mobilization in Tertiary Polymer Flood

A negligible (if any) amount of oil was produced (determined from the produced fluids) in experiments 1–3 where elastic polymer 1 (low salinity) was used for the tertiary flood. The oil saturation increase of 2.0%–2.7% at the end of the tertiary flood (Figure 5 – #1–#3) was caused by the oil swelling (non-monotonic) due to the emulsion generation in the oil ganglia. The swelling and *saturation increase* are visually demonstrated in the zoomed-in cross-section (in the middle of the chip to avoid entrance/end effects) in Figures 8c, 8d and 8e. Oil ganglia redistribution in the transverse direction was observed, as indicated by the locations of the green (mobilized) and blue colors (newly occupied) in Figure 8e. Ganglia swelling and redistribution reduced the ganglia number and changed the ganglia morphology. In the cross-section from Figure 8c to Figure 8d, the oil saturation increased from 30% to 32% due to ganglia swelling, and the number of oil ganglia decreased by 7.7% as a result of redistribution and reconnection induced by swelling. Obvious ganglia transverse redistribution and swelling were repeatedly observed from experiments 2 to 3 which are included in the supporting information Section S5.

Due to the oil swelling and the later partial de-swelling in experiments 1–3, the oil saturation increased then decreased. The peak saturation increase was 5.6%, 7.0%, and 5.8%, higher than the saturation increase at the end of tertiary flood which was 2.4%, 2.0%, and 2.7%, respectively (Figure 5 – #1–#3). The number of oil ganglia first decreased then increased but was lower after than prior to the polymer flood. Supplemental figures regarding this oil swelling saturation process are included in the supporting information Section S4.

In Experiment 4 where elastic polymer 2 (high salinity) was used for the tertiary flood, oil started to mobilize and was produced upon switching to polymer flood, and a saturation reduction of 2% was obtained (Figure 5 – #4). The oil saturation did not change at any point except the decrease due to oil production, and no ganglia swelling was observed (Figures 9c, 9d and 9e). Many small to moderate oil ganglia were entirely recovered, while some larger ones were broken down and/or partially recovered (Figure 9e). In the cross-section from Figure 9c to Figure 9d, the oil saturation decreased from 21% to 17% due to mobilization, and the ganglia number increased by 7.8% as a result of ganglia break-up. More details regarding the oil mobilization process (not relevant to the mechanisms discussed in this study) are included in the supporting information Section S6.

In experiments 5 and 6 where inelastic polymer 1 (high salinity) was used for the tertiary flood, no oil was produced from the outlet of the micromodel. The oil saturation remained unchanged as seen from the saturation plots (Figure 5 – #5, #6). The oil in the micromodel was already at residual saturation resulting from the secondary glycerol flood, therefore, a conventional inelastic polymer flood cannot recover residual oil by improving macroscopic sweep efficiency which agrees with fractional flow theory (Lake et al., 2014). Additional analysis of this process is included in the supporting information Section S7.

In experiments 7 and 8 where inelastic polymer 2 (low salinity) was used for the tertiary flood, no oil was produced from the outlet of the micromodel. Similar to experiments 1–3, oil saturation increased by 4.0% and 3.8% for experiments 7 and 8 (Figure 5 – #7, #8), respectively, which was caused by ganglia swelling (Figures 10c, 10d and 10e). Unlike experiments 1–3, redistribution of oil was not observed, as residual oil ganglia enlarged around their original locations and barely moved indicated by the lack of green color (mobilized; Figure 10e). In the cross-section from Figure 10c to Figure 10d, the oil saturation increased from 30% to 36% due to ganglia swelling, and the ganglia number slightly decreased by 3.6% as a result of the ganglia reconnection induced by swelling.

4.2.2. Residual Ganglia Mobilization in Post-Tertiary Viscous Aqueous Phase Flood

In experiments 1–3 where elastic polymer 1 was used in the previous tertiary flood, saturation decrease (of 6.4%, 3.0%, and 7.3%, respectively) with oil mobilization (Figure 11a) and recovery were observed. The

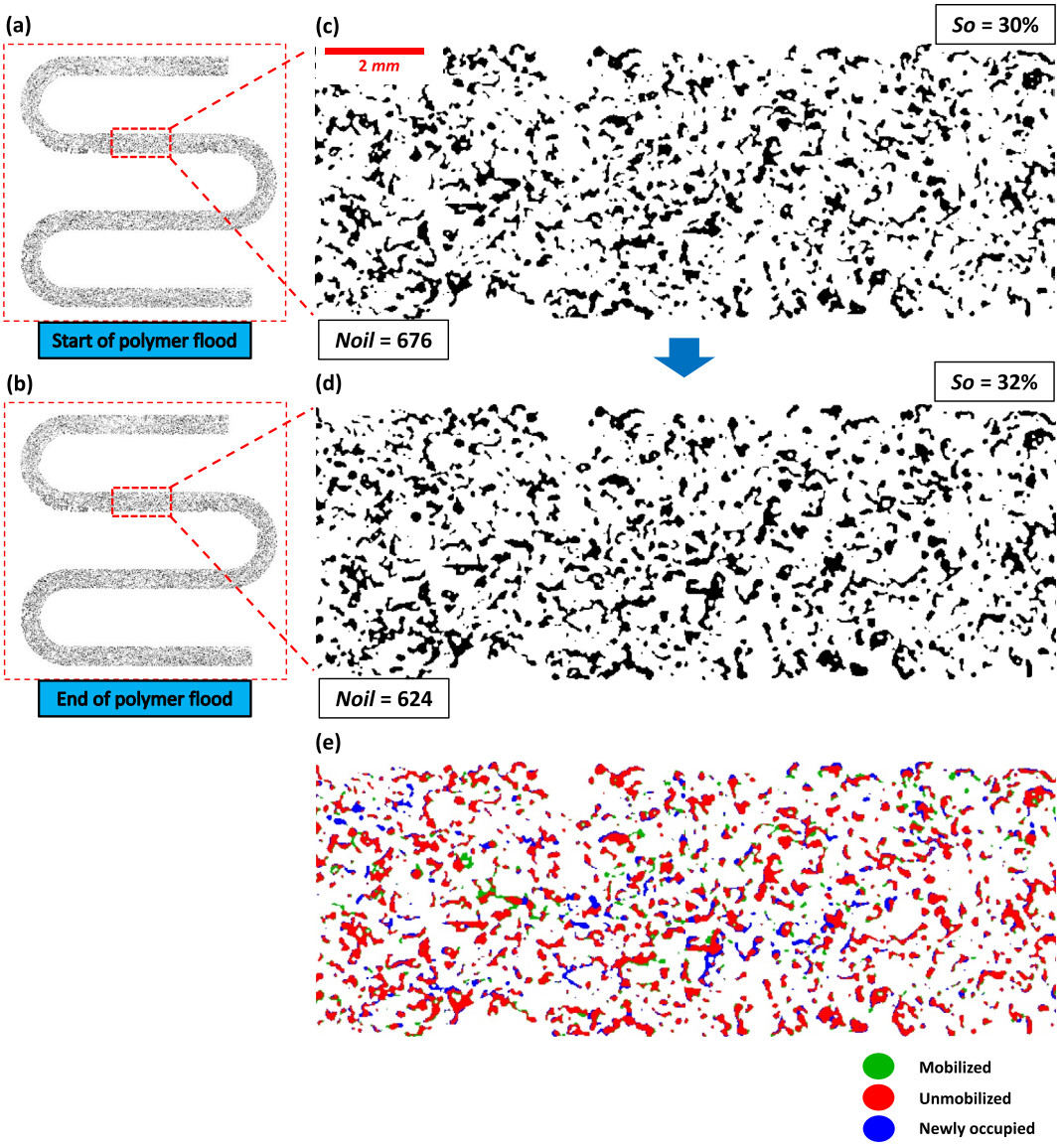

Figure 8. Oil swelling and redistribution during tertiary polymer flood in Experiment 1 (high elasticity and low salinity). Entire domain is shown at (a) the beginning of polymer flood and (b) the end of polymer flood. (c) and (d) are the same cross-section zoomed-in from (a) and (b), respectively. (e) Changes from (c) to (d). The green, red and blue colors represent the mobilized, unmobilized, and newly occupied oil ganglia, respectively.

saturation decrease and oil mobilization both began immediately after starting the flood. The saturation decrease continued for ~1.0 pore volume of injection, starting with a gradual decrease followed by a more abrupt decline. The combined oil saturation changes in the tertiary and the post-tertiary floods indicated a net oil saturation decrease (of 4.0%, 1.0%, and 4.8%, respectively). The actual net oil recovery due to elasticity should be higher than the net saturation reduction, because the oil de-swelling cannot completely compensate the prior swelling (see experiments 7 and 8), therefore the remaining oil saturation was higher than its original state.

In Experiment 4 where elastic polymer 2 was used in the previous tertiary flood, saturation decrease (of 5%) entirely from residual oil mobilization and recovery, and not de-swelling, were observed (Figure 11b). The saturation decrease and oil mobilization both began immediately after starting the flood. The decline trend was similar to that in experiments 1–3, as the saturation decrease continued for ~1.0 pore volume of injection, starting with a gradual decrease followed by a more abrupt decline. The combined oil saturation

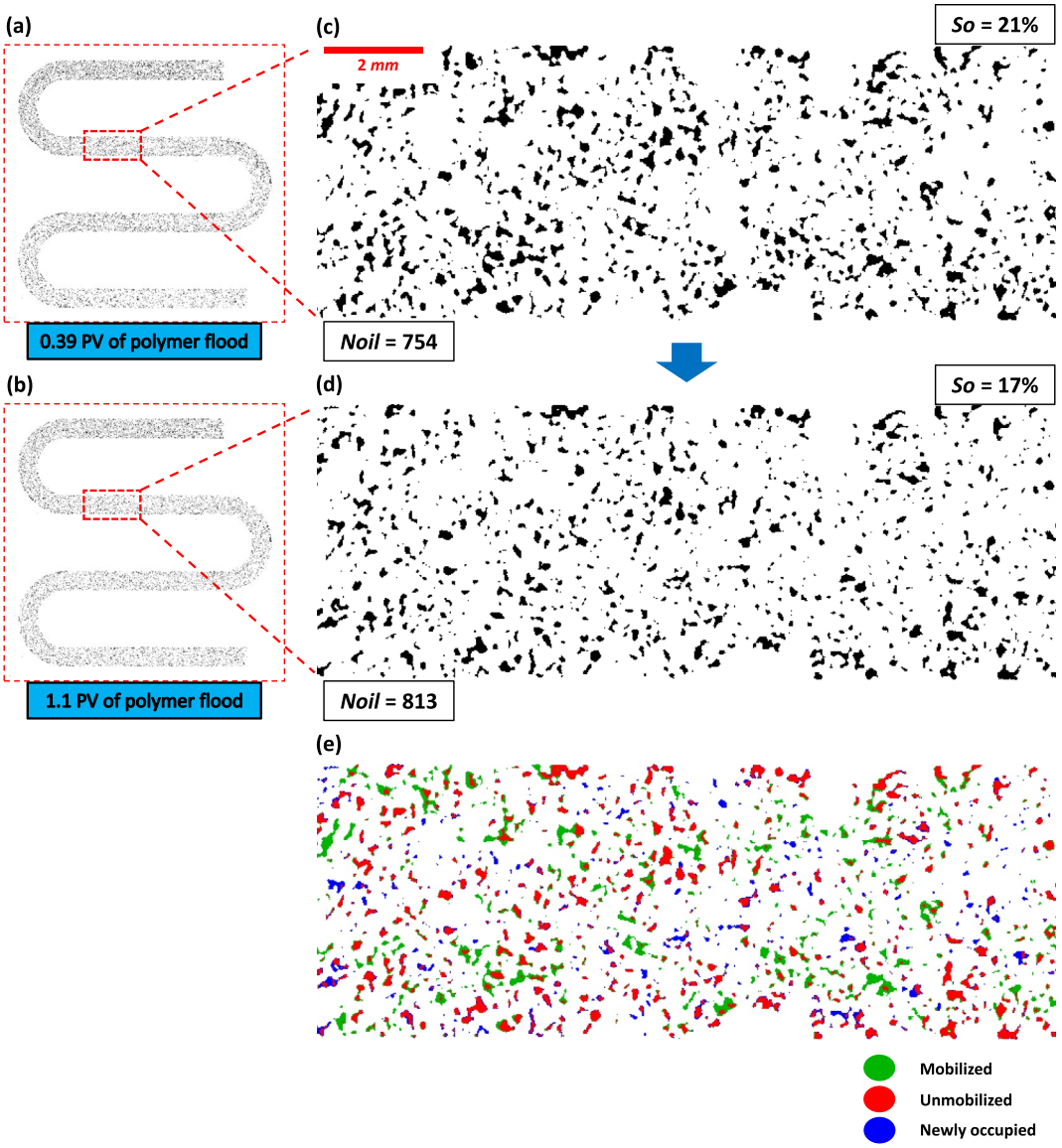

Figure 9. Oil mobilization during tertiary polymer flood in Experiment 4 (high elasticity and high salinity). Entire domain is shown at (a) 0.39 pore volumes of polymer flood (before oil mobilization) and (b) 1.1 pore volumes of polymer flood (after oil mobilization). (c) and (d) are the same cross-section zoomed-in from (a) and (b), respectively. (e) Changes from (c) to (d). The green, red, and blue colors represent the mobilized, unmobilized, and newly occupied oil ganglia, respectively.

changes in the tertiary and the post-tertiary floods indicated a net oil saturation decrease (of 7.0%), which is the total saturation reduction caused by elasticity.

In experiments 5 and 6 where inelastic polymer 1 was used in the previous tertiary flood, no saturation decrease or oil recovery were observed. The oil saturation remained almost unchanged (Figure 5 – #5, #6) and no oil production from the outlet was observed.

In experiments 7 and 8 where inelastic polymer 2 was used in the previous tertiary flood, a slight, gradual saturation decrease (of 0.8% and 2.2%, respectively) without oil recovery or mobilization were observed. The oil saturation decrease was completely from the oil ganglia de-swelling and negligible mobilization was observed (Figure 11c). The final oil saturation was higher than before the tertiary polymer flood, described by a net saturation increase (of 3.2% and 1.7%, respectively), indicating that the de-swelling did not completely compensate for the prior swelling.

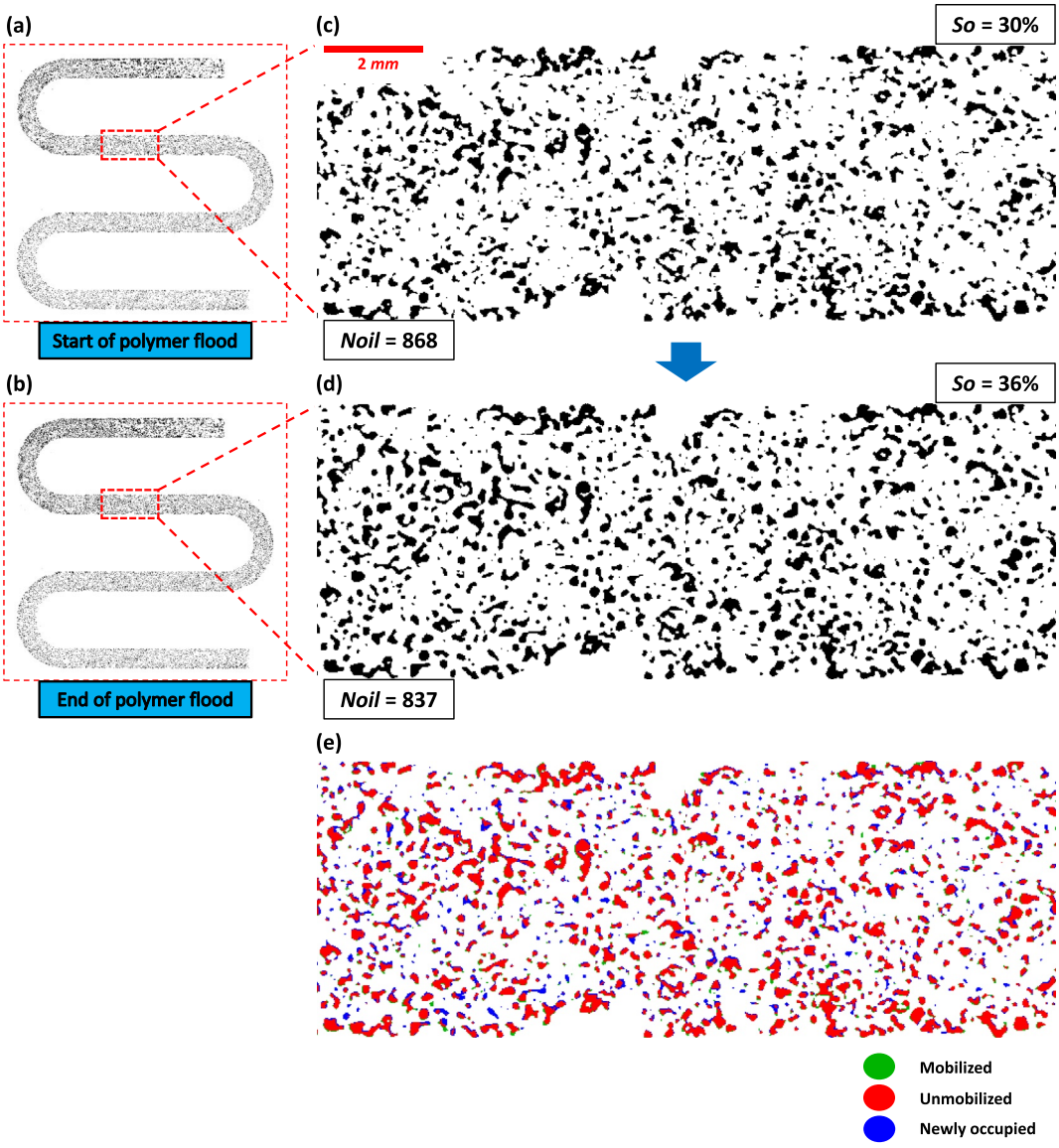

Figure 10. Oil swelling during tertiary polymer flood in Experiment 7 (low elasticity and low salinity). Entire domain is shown at (a) the beginning of polymer flood and (b) the end of polymer flood. (c) and (d) are the same cross-section zoomed-in from (a) and (b), respectively. (e) Changes from (c) to (d). The green, red and blue colors represent the mobilized, unmobilized, and newly occupied oil ganglia, respectively.

4.3. Mechanistic Discussion

4.3.1. Elasticity Induced Redistribution/Mobilization & Salinity Related Ganglia Swelling

With either high or low salinity, the high-elasticity polymers redistribute the residual ganglia and ultimately lead to residual oil recovery mainly through the post-tertiary flood. Low salinity plays a role supplemental to elasticity, but did not significantly impact the relationship between the ultimate oil recovery and elasticity (Figure 6b). Low salinity polymers cause ganglia swelling which contribute to reconnection. Swelling and reconnection, which reduce the capillary trapping force and make mobilization relatively easier, are minor effects on residual saturation reduction compared with redistribution. Swelling may add to redistribution through morphology changes, but is a minor effect on redistribution compared to elasticity (also see the supporting information Section S4).

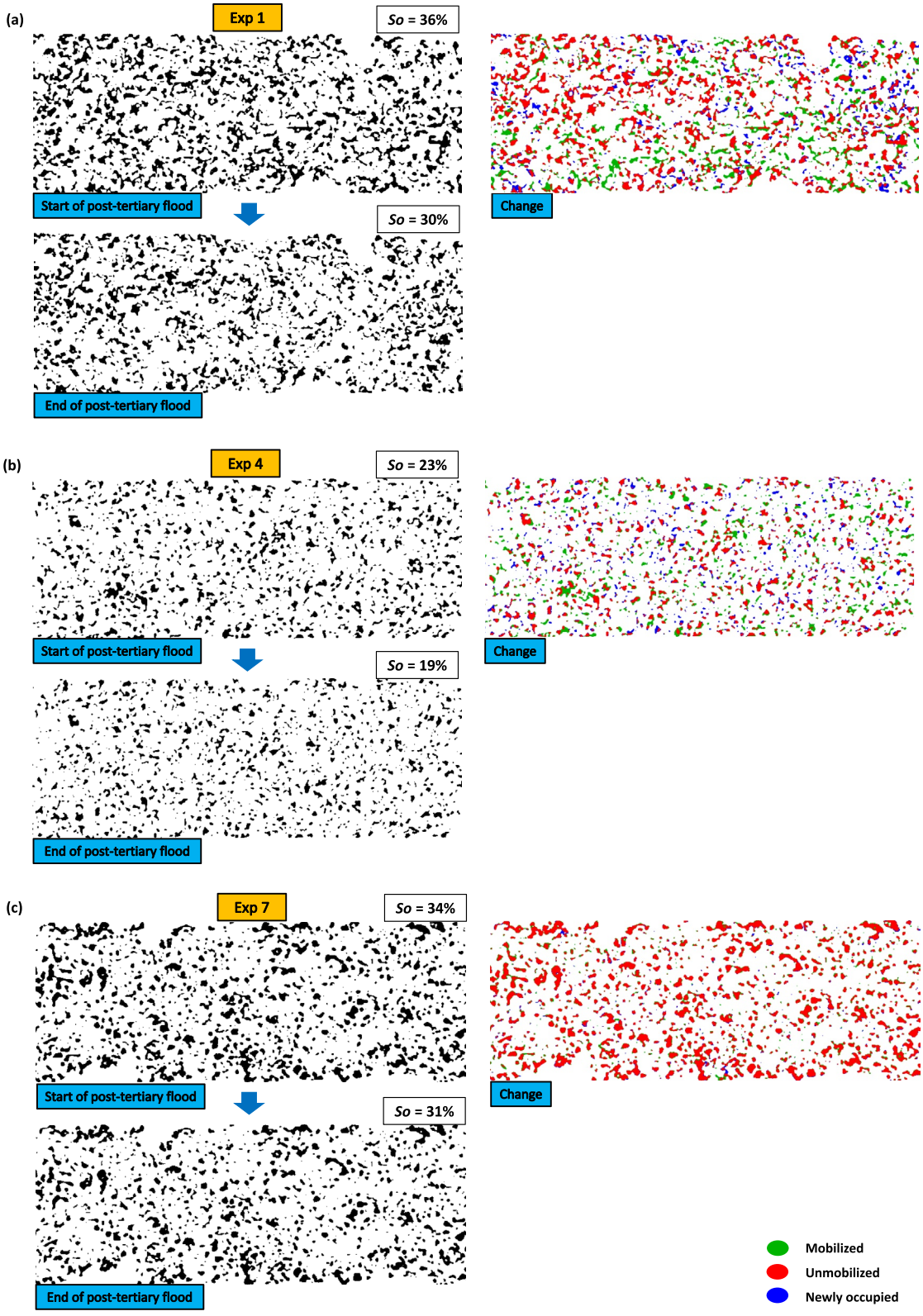

Figure 11. Oil saturation and distribution changes in a cross-section during post-tertiary glycerol flood in (a) experiments 1 (high elasticity and low salinity), (b) Experiment 4 (high elasticity and high salinity), and (c) Experiment 7 (low elasticity and low salinity). The green, red, and blue colors represent the mobilized, unmobilized, and newly occupied oil ganglia, respectively.

The low polymer salinity induced non-monotonic ganglia swelling has not been revealed in previous works. The observed water-in-oil emulsions are not shear-induced where the emulsion stability increases with salinity (Ling et al., 2018), but are generated spontaneously during the oil/water contact at low flow/shear and static conditions as shown in the supporting information Section S3. In the static experiment (see the supporting information Section 3), the crude oil was directly contact with inelastic polymer 1 (low salinity), and water-in-oil emulsions and oil swelling were observed. The oil ganglion swelling rate versus the contacting time with the low salinity polymer solution is analyzed. We did not investigate the emulsion stability after the spontaneous formation of the emulsions in this work.

The spontaneous emulsion is also not induced by the traditional *low salinity effects* (improved recovery due to low invading aqueous phase salinity) described in previous studies (Du et al., 2019; Tetteh et al., 2020; Wu & Firoozabadi, 2021) in terms of occurrence, process, and consequences. For the occurrence, low salinity aqueous solutions flood did not cause emulsions or swelling before or after the polymer flood (Figure 7) but could have with traditional *low salinity effects*. In addition, the emulsions and swelling occurred immediately after switching to polymer flood which contradict previous observations of the *slow process* that takes tens of hours to days to progress (Du et al., 2019; Sandengen et al., 2016; Sohrabi et al., 2017). In the process, chemical potential difference (between water components) induced spontaneous mass transfer between phases may occur (De Gennes & Taupln, 1982; Lemaire et al., 1983), but cannot sufficiently explain the non-monotonicity. As to the consequences, no recovery was obtained when the low salinity, low-elasticity polymer was used, and the initial wettability with oil and glycerol solutions was already water-wet (Figure 1e). The *in-situ* contact angle between oil and the glycerol solution before secondary flood and after post-tertiary flood (with different polymers used in the prior tertiary floods) did not show significant difference in different cases (see the supporting information Figure S9). Therefore, the system stayed water-wet in the process. Both evidences exclude the occurrence of *low salinity effects* and their wettability alteration (from oil-wet to water-wet) induced saturation reduction. In summary, this salinity related swelling is a combined effect of the salinity and the specific polymer properties, which needs further investigation.

Polymer salinity appears to affect the IFT with crude oil, as the IFT of the high salinity polymer/oil is an order of magnitude lower than that of low salinity polymers/oil (Table 2), but IFT is not a significant contributor to the elasticity induced residual saturation reduction. The two polymers with similar, low IFT values (elastic polymer 2 and inelastic polymer 1) show qualitatively different behaviors because of the elasticity difference.

4.3.2. Comparison and Discussion With Existing Studies

A considerable amount of residual oil recovery was obtained in the post-tertiary flood that followed the high-elasticity polymer floods (regardless of the polymer salinity) in the *coreflood-on-a-chip*. The ultimate residual saturation reduction from our 2.5D, *coreflood-on-a-chip* experiments is ∼5% of the total pore volume, which is consistent with previous results from coreflood experiments (Jin et al., 2020; Qi et al., 2017). The post-tertiary low-elasticity polymers also further reduce the residual oil saturation in corefloods (Erincik et al., 2018; Jin et al., 2020). It indicates that the microscopic ganglia redistribution and morphology changes, although occur immediately, have long-term effects on mobilization and residual saturation reduction. It can be inferred that *residual saturation* is affected by microscopic distribution and fluid morphology, which play the dominant role in further saturation reduction after the high-elasticity flood. Existing analyses of the microscopic redistribution and morphology changes of the NAPL/oil ganglia in rock samples during fluid-fluid displacement have provided enormous amount of related evidence (Berg et al., 2013; Gao et al., 2020; Lin et al., 2019; Reynolds et al., 2017).

The observed residual fluid redistribution can be related to the flow field fluctuation or ganglia oscillation during viscoelastic flow as demonstrated in 2D micromodel experiments (Clarke et al., 2015) and by pore-scale simulation in a pore-throat geometry (Xie et al., 2020). The correlation of neighboring pores (e.g., the pore spacing) may contribute to the ganglion redistribution and mobilization within and between pores, by forming unstable eddies in the corners of the pore bodies under unstable flow with proper pore spacing (Browne et al., 2020a). In this study, we did not measure the flow field in the *coreflood-on-a-chip* model as conducted in the mentioned works (Browne et al., 2020a; Clarke et al., 2015), which could be an important component in our future study.

In this work, residual oil reduction was mainly obtained from the post-tertiary flood although the redistribution occurred in tertiary high-elasticity flood. Previous microfluidic studies rarely reported reduction in residual oil saturation, and corefloods obtained considerable amounts of saturation reduction in tertiary high-elasticity polymer flood (Qi et al., 2017; Vermolen et al., 2014). Geometric differences (e.g., cross-section topology) may explain the different observations, by affecting the transverse redistribution and impacting on flow dynamics. The limited amount of redistribution restricted by the cross-sectional dimension of micromodels caused the lack or delay of the mobilization/recovery, but can lead to residual recovery when redistribution is high in real rocks. Limitations of this work are discussed in the supporting information Section S11.

There is a concern with using traditional microfluidics to investigate fluid transport in porous media, because the observation and analysis obtained in a small geometry are sometimes not applicable to larger scales. For example, capillary end effects may impact the distribution of fluids and the displacement processes (Huang & Honarpour, 1998; Kang & Yun, 2018; Tanino & Christensen, 2019). In addition, the redistribution, mobilization, and re-trapping of capillary-trapped residual oil are also impacted by the spatial scale and topology of the flow geometries, which explains the lack of direct evidence in previous microfluidic studies. Therefore, this work contributes to general pore-scale, fundamental investigation of fluid dynamics in porous media through the implementation of a long, REV-scale porous media without compromising the advantageous features of microfluidics. This work, therefore, provides an important benchmark example of using such *coreflood-on-a-chip* method and potentially will have long-term impacts in the area of water resources studies.

5. Conclusions

Coreflood-on-a-chip experiments were conducted to explore the role of viscoelasticity in reducing residual fluid saturation, which has been observed, but not well explained, in literature studying NAPL/oil recovery. We isolate the effects of viscosity and salinity from elasticity, by conducting a secondary flood and a post-tertiary flood with high viscosity Newtonian fluid before and after polymer flood, respectively. This work overall demonstrates that (a) viscoelasticity does help in reducing the residual NAPL/oil saturation without posing extraordinal large viscous force, as flow instabilities resulted from viscoelastic flow induce reconnection and redistribution of residual ganglia; and (b) low salinity enhances the residual fluid reconnection and redistribution by swelling residual ganglia, therefore enhances the residual fluid recovery when elasticity is high. Systematic screening experiments indicate:

- Recovery of residual fluid occurs only when tertiary flood is of high elasticity. In addition, the recovery is mainly observed after the tertiary flood, during the post-tertiary, inelastic flood. No recovery of residual fluid is observed during tertiary or post-tertiary flood when the polymer is of low elasticity.
- Microscopic observation and ganglia-scale statistics reveal that high elastic polymer flood triggers the redistribution and reconnection of residual ganglia, which allows additional recovery of residual fluid in the post-tertiary flood by viscous Newtonian fluid. The reconnection and redistribution of residual fluid are attributed to flow instabilities during the viscoelastic fluid flood.
- An increase of apparent residual fluid saturation during tertiary flood is always observed under low salinity condition. Microscopic observation reveals that low salinity induces spontaneous emulsification and therefore apparent "swelling" of oil. This swelling effect makes the reconnection of residual ganglia easier, and also contributes to the increase of apparent residual fluid saturation.
- Low salinity enhances the recovery of residual fluid when high-elasticity polymer flood is performed. However, low salinity does not impact recovery when the tertiary flood is conducted with low-elasticity polymer.

Appendix A

To estimate the apparent viscosity of polymers in the experiments, shear rate in porous media at the experimental conditions is estimated using an empirical equation (Koh et al., 2018):

$$\dot{\gamma} = C\left(\frac{3n+1}{4n}\right)^{\frac{n-1}{n}} \frac{4}{\sqrt{8}} \frac{u_w}{\sqrt{KK_{rw}\emptyset S_w}} \tag{A1}$$

where C is the shear correction factor for the porous medium and is generally taken to be 4.0 (Koh et al., 2018), n is the shear-thinning index, u_w is the Darcy velocity of the aqueous phase, K is thepermeability, K_{rw} is the relative permeability of aqueous phase, $\emptyset$ is the porosity, and S_w is the aqueous phase saturation (glycerol and polymer solutions). A value of 0.1 was used as aqueous phase relative permeability in the water-wet porous media as obtained from many published results (Erincik et al., 2018; Jin et al., 2020; Qi et al., 2017), and aqueous phase saturation at the end of secondary flood experiments 1–8 were used for S_w. Using Equation A1, the shear rates and the corresponding viscosities are determined for each of the polymer solutions at the experimental conditions (Table 2). The estimated shear rates of different polymers in different experiments vary in a reasonably range, and the corresponding apparent viscosities are similar but all of them are lower than the viscosities of the glycerol solutions (Figure 2a).

Deborah number (*De*), a dimensionless number that describes the ratio of elastic to viscous forces, is defined in this work by:

$$De = \tau_r \dot{\gamma} \tag{A2}$$

where τ_r is the relaxation time, and $\dot{\gamma}$ is the shear rate. More discussion on elasticity and the estimation of *De* is included in the supporting information Section S12.

Nomenclature

C	shear correction factor for the porous medium
Ca	capillary number
De	Deborah number
2.5D	two and half dimensional
3D	three dimensional
G'	storage modulus
G''	loss modulus
HPAM	partially hydrolyzed polyacrylamide
K	permeability
K_{rw}	aqueous phase relative permeability
n	shear-thinning index
NAPL	nonaqueous phase fluid
$Noil$	oil ganglia number
Re	Reynold number
S_o	oil saturation
S_w	aqueous phase saturation
$\dot{\gamma}$	shear rate (s^{-1})
u	viscosity (cp)
τ_r	relaxation time (s)
$\emptyset$	porosity

Data Availability Statement

Data generated for this study can be accessed from Texas Data Repository (https://dataverse.tdl.org/dataverse/Du_et_al_WRR_2021).

Acknowledgment
The authors would like to thank the sponsors of the Chemical EOR Industrial Affiliates Research Project in the Center for Subsurface Energy and the Environment at the University of Texas at Austin for their support. The authors are grateful for Ultimate EOR Services LLC for allowing us to use their laboratory equipment.

References

Anbari, A., Chien, H. T., Datta, S. S., Deng, W., Weitz, D. A., & Fan, J. (2018). Microfluidic model porous media: Fabrication and applications. *Small*, *14*(18), 1703575. https://doi.org/10.1002/smll.201703575

Berg, S., Ott, H., Klapp, S. A., Schwing, A., Neiteler, R., Brussee, N., et al. (2013). Real-time 3D imaging of Haines jumps in porous media flow. *Proceedings of the National Academy of Sciences*, *110*(10), 3755–3759. https://doi.org/10.1073/pnas.1221373110

Blunt, M. J., Bijeljic, B., Dong, H., Gharbi, O., Iglauer, S., Mostaghimi, P., et al. (2013). Pore-scale imaging and modeling. *Advances in Water Resources*, *51*, 197–216. https://doi.org/10.1016/j.advwatres.2012.03.003

Browne, C. A., Shih, A., & Datta, S. S. (2020a). Bistability in the unstable flow of polymer solutions through pore constriction arrays. *Journal of Fluid Mechanics*, *890*. https://doi.org/10.1017/jfm.2020.122

Browne, C. A., Shih, A., & Datta, S. S. (2020b). Pore-scale flow characterization of polymer solutions in microfluidic porous media. *Small*, *16*(9), 1903944. https://doi.org/10.1002/smll.201903944

Castelletto, V., Hamley, I. W., Xue, W., Sommer, C., Pedersen, J. S., & Olmsted, P. D. (2004). Rheological and structural characterization of hydrophobically modified polyacrylamide solutions in the semidilute regime. *Macromolecules*, *37*(4), 1492–1501. https://doi.org/10.1021/ma035039d

Chen, D. T. N., Wen, Q., Janmey, P. A., Crocker, J. C., & Yodh, A. G. (2010). Rheology of soft materials. *Annual Review of Condensed Matter Physics*, *1*, 301–322. https://doi.org/10.1146/annurev-conmatphys-070909-104120

Clarke, A., Howe, A. M., Mitchell, J., Staniland, J., & Hawkes, L. A. (2016). How viscoelastic-polymer flooding enhances displacement efficiency. *SPE Journal*, *21*(3), 675–0687. SPE-174654-PA. https://doi.org/10.2118/174654-PA

Clarke, A., Howe, A. M., Mitchell, J., Staniland, J., Hawkes, L. A., & Leeper, K. (2015). Mechanism of anomalously increased oil displacement with aqueous viscoelastic polymer solutions. *Soft Matter*, *11*, 3536–3541. https://doi.org/10.1039/C5SM00064E

de Castro, R., Shokri, A. N., Karadimitriou, N., Oostrom, M., & Joekar-Niasar, V. (2015). Experimental study on nonmonotonicity of capillary desaturation curves in a 2-D pore network. *Water Resources Research*, *51*(10), 8517–8528. https://doi.org/10.1002/2015wr017727. http://doi.org/10.1002/2015WR017727

De Gennes, P. G., & Taupln, C. (1982). Microemulsions and the flexibility of oil/water interfaces. *The Journal of Physical Chemistry*, *86*(13), 2294–2304. https://doi.org/10.1021/j100210a011

Delshad, M., Kim, H. D., Magbagbeola, O. A., Huh, C., Pope, G. A., & Tarahhom, F. (2008). Mechanistic interpretation and utilization of viscoelastic behavior of polymer solutions for improved polymer-flood efficiency. In *Presented at SPE Symposium on Improved Oil Recovery, 20-23 April, Tulsa, Oklahoma, USA*. SPE-113620-MS. https://doi.org/10.2118/113620-MS

Du, Y., Mehmani, A., Xu, K., Kelly, S., Balhoff, M. T., & Torres-Verdín, C. (2020). Microfluidic diagnostics of the impact of local microfracture connectivity on hydrocarbon recovery following water injection. *Water Resources Research*, *56*(7), e2019WR026944. https://doi.org/10.1029/2019WR026944

Du, Y., Xu, K., Mejia, L., Zhu, P., & Balhoff, M. (2019). Microfluidic investigation of low-salinity effects during oil recovery: A no-clay and time-dependent mechanism. *SPE Journal*, *24*(06), 2841–2858. SPE-197056-PA. https://doi.org/10.2118/197056-PA

Erincik, M. Z., Qi, P., Balhoff, M. T., & Pope, G. A. (2018). New method to reduce residual oil saturation by polymer flooding. *SPE Journal*, *23*(05), 1944–1956. SPE-187230-PA. https://doi.org/10.2118/187230-PA

Farajzadeh, R., Bedrikovetsky, P., Lotfollahi, M., & Lake, L. W. (2015). Simultaneous sorption and mechanical entrapment during polymer flow through porous media. *Water Resources Research*, *52*(3), 2279–2298. https://doi.org/10.1002/2015WR017885

Frollini, E., Piscitelli, D., VerginellI, I., Baciocchi, R., & Petitta, M. (2016). A methodological approach to assess the dissolution of residual LNAPL in saturated porous media and its effect on groundwater quality: Preliminary experimental results. *Water, Air, & Soil Pollution*, *227*, 379. https://doi.org/10.1007/s11270-016-3077-7

Gao, Y., Lin, Q., Bijeljic, B., & Blunt, M. J. (2017). X-ray microtomography of intermittency in multiphase flow at steady state using a differential imaging method. *Water Resources Research*, *53*(12), 10274–10292. https://doi.org/10.1002/2017WR021736

Gao, Y., Raeini, A. Q., Selem, A. M., Bondino, I., Blunt, M. J., & Bijeljic, B. (2020). Pore-scale imaging with measurement of relative permeability and capillary pressure on the same reservoir sandstone sample under water-wet and mixed-wet conditions. *Advances in Water Resources*, *146*, 103786. https://doi.org/10.1016/j.advwatres.2020.103786

Geller, J. T., & Hunt, J. R. (1993). Mass transfer from nonaqueous phase organic liquids in water-saturated porous media. *Water Resources Research*, *29*(4), 833–845. https://doi.org/10.1029/92WR02581

Ghosh, J., Ticka, G. R., Akyol, N. H., & Zhang, Y. (2019). A pore-scale investigation of heavy crude oil trapping and removal during surfactant-enhanced remediation. *Journal of Contaminant Hydrology*, *223*, 103471. https://doi.org/10.1016/j.jconhyd.2019.03.003

Groisman, A., & Steinberg, V. (2000). Elastic turbulence in a polymer solution flow. *Nature*, *405*, 53–55. https://doi.org/10.1038/35011019

Hirasaki, G. J., & Pope, G. A. (1974). Analysis of factors influencing mobility and adsorption in the flow of polymer solution through porous media. *SPE Journal*, *14*(04), 337–346. SPE-4026-PA. https://doi.org/10.2118/4026-PA

Ho, T. C., & Denn, M. M. (1977). Stability of plane Poiseuille flow of a highly elastic liquid. *Journal of Non-Newtonian Fluid Mechanics*, *3*(2), 179–195. https://doi.org/10.1016/0377-0257(77)80048-7

Hu, R., Wan, J., Kim, Y., & Tokunaga, T. K. (2017). Wettability impact on supercritical CO_2 capillary trapping: Pore-scale visualization and quantification. *Water Resources Research*, *53*(8), 6377–6394. https://doi.org/10.1002/2017WR020721

Huang, D. D., & Honarpour, M. M. (1998). Capillary end effects in coreflood calculations. *Journal of Petroleum Science and Engineering*, *19*(1–2), 103–117. https://doi.org/10.1016/S0920-4105(97)00040-5

Huh, C., & Pope, G. A. (2008). Residual oil saturation from polymer floods: Laboratory measurements and theoretical interpretation. In *SPE Symposium on Improved Oil Recovery, 20-23 April, Tulsa, Oklahoma, USA*. SPE-113417-MS. https://doi.org/10.2118/113417-MS

Imhoff, P. T., Farthing, M. W., Gleyzer, S. N., & Miller, C. T. (2002). Evolving interface between clean and nonaqueous phase liquid (NAPL)-contaminated regions in two-dimensional porous media. *Water Resources Research*, *38*(6), 307–311. https://doi.org/10.1029/2001WR000290

Imhoff, P. T., Jaffé, P. R., & Pinder, G. F. (1994). An experimental study of complete dissolution of a nonaqueous phase liquid in saturated porous media. *Water Resources Research*, *30*(2), 307–320. https://doi.org/10.1029/93WR02675

Jin, J., Qi, P., Mohanty, K., & Balhoff, M. (2020). Experimental investigation of the effect of polymer viscoelasticity on residual saturation of low viscosity oils. In *Presented at SPE Improved Oil Recovery Conference, 31 August-4 September, Tulsa, Oklahoma, USA*. SPE-200414-MS. https://doi.org/10.2118/200414-MS

Jin, M., Hirasaki, G. J., Jackson, R. E., Kostarelos, K., & Pope, G. A. (2007). Control of downward migration of dense nonaqueous phase liquid during surfactant flooding by design simulations. *Water Resources Research*, *43*(1). https://doi.org/10.1029/2006WR004858

Johns, M. L., & Gladden, L. F. (2000). Probing ganglia dissolution and mobilization in a water-saturated porous medium using MRI. *Journal of Colloid and Interface Science*, *225*(1), 119–127. https://doi.org/10.1006/jcis.2000.6742

Johns, M. L., & Gladden, L. F. (2001). Surface-to-volume ratio of ganglia trapped in small-pore systems determined by pulsed-field gradient nuclear magnetic resonance. *Journal of Colloid and Interface Science*, *238*(1), 96–104. https://doi.org/10.1006/jcis.2001.7494

Kang, D. H., & Yun, T. S. (2018). Minimized capillary end effect during CO_2 displacement in 2-D micromodel by manipulating capillary pressure at the outlet boundary in lattice Boltzmann method. *Water Resources Research*, *54*(2), 895–915. https://doi.org/10.1002/2017WR021409

Koh, H., Lee, V. B., & Pope, G. A. (2018). Experimental investigation of the effect of polymers on residual oil saturation. *SPE Journal*, *23*(01), 1–17. SPE-179683-PA. https://doi.org/10.2118/179683-PA

Lake, L. W., Johns, R., Rossen, B., & Pope, G. (2014). *Fundamentals of enhanced oil recovery*. Society of Petroleum Engineers.

Larson, R. G. (1992). Instabilities in viscoelastic flows. *Rheologica Acta*, *31*, 213–263. https://doi.org/10.1007/BF00366504

Lemaire, B., Bothorel, P., & Roux, D. (1983). Micellar interactions in water-in-oil microemulsions. 1. Calculated interaction potential. *The Journal of Physical Chemistry*, *87*(6), 1023–1028. https://doi.org/10.1021/j100229a021

Li, X., Berg, S., Castellanos-Diaz, O., Wiegmann, A., & Verlaan, M. (2020). Solvent-dependent recovery characteristic and asphaltene deposition during solvent extraction of heavy oil. *Fuel*, *263*, 116716. https://doi.org/10.1016/j.fuel.2019.116716

Lifton, V. A. (2016). Microfluidics: An enabling screening technology for enhanced oil recovery (EOR). *Lab on a Chip*, *16*, 1777–1796. https://doi.org/10.1039/C6LC00318D

Lin, Q., Bijeljic, B., Berg, S., Pini, R., Blunt, M. J., & Krevor, S. (2019). Minimal surfaces in porous media: Pore-scale imaging of multiphase flow in an altered-wettability Bentheimer sandstone. *Physical Review E*, *99*, 063105. https://doi.org/10.1103/PhysRevE.99.063105

Ling, N. N. A., Haber, A., Graham, B. F., Aman, Z. M., May, E. F., Fridjonsson, E. O., & Johns, M. L. (2018). Quantifying the effect of salinity on oilfield water-in-oil emulsion stability. *Energy & Fuels*, *32*(9), 10042−10049. https://doi.org/10.1021/acs.energyfuels.8b02143

Mehmani, A., Kelly, S., & Torres-Verdín, C. (2020). Leveraging digital rock physics workflows in unconventional petrophysics: A review of opportunities, challenges, and benchmarking. *Journal of Petroleum Science and Engineering*, *190*, 107083. https://doi.org/10.1016/j.petrol.2020.107083

Mehmani, A., Kelly, S., Torres-Verdín, C., & Balhoff, M. (2019). Capillary trapping following imbibition in porous media: Microfluidic quantification of the impact of pore-scale surface roughness. *Water Resources Research*, *55*(11), 9905–9925. https://doi.org/10.1029/2019WR025170

Mejia, L., Tagavifar, M., Xu, K., Mejia, M., Du, Y., & Balhoff, M. (2019). Surfactant flooding in oil-wet micromodels with high permeability fractures. *Fuel*, *241*(1), 1117–1128. https://doi.org/10.1016/j.fuel.2018.12.076

Mejia, L., Zhu, P., Hyman, J. D., Mohanty, K. K., & Balhoff, T. M. (2020). Coreflood on a chip: Core-scale micromodels for subsurface applications. *Fuel*, *281*(1), 118716. https://doi.org/10.1016/j.fuel.2020.118716

Mitchell, J., Lyons, K., Howe, A. M., & Clarke, A. (2016). Viscoelastic polymer flows and elastic turbulence in three-dimensional porous structures. *Soft Matter*, *12*, 460–468. https://doi.org/10.1039/c5sm01749a

Mohagheghi, M., & Khomami, B. (2016). Elucidating the flow-microstructure coupling in the entangled polymer melts. Part I: Single chain dynamics in shear flow. *Journal of Rheology*, *60*, 849–859. https://doi.org/10.1122/1.4961481

Morozov, A. N., & van Saarloos, W. (2007). An introductory essay on subcritical instabilities and the transition to turbulence in visco-elastic parallel shear flows. *Physics Reports*, *447*(3–6), 112–143. https://doi.org/10.1016/j.physrep.2007.03.004

Phenrat, T., Fagerlund, F., Illangasekare, T., Lowry, G. V., & Tilton, R. D. (2011). Polymer-modified Fe^0 nanoparticles target entrapped NAPL in two dimensional porous media: Effect of particle concentration, NAPL saturation, and injection strategy. *Environmental Science and Technology*, *45*(14), 6102–6109. https://doi.org/10.1021/es200577n

Philippe, N., Davarzani, H., Colombano, S., Dierick, M., Klein, P.-Y., & Marcoux, M. (2020). Experimental study of the temperature effect on two-phase flow properties in highly permeable porous media: Application to the remediation of dense non-aqueous phase liquids (DNAPLs) in polluted soil. *Advances in Water Resources*, *146*, 103783. https://doi.org/10.1016/j.advwatres.2020.103783

Qi, P. (2018). *The effect of polymer viscoelasticity on residual oil saturation*. Ph.D. dissertation. University of Texas at Austin.

Qi, P., Ehrenfried, D. H., Koh, H., & Balhoff, M. T. (2017). Reduction of residual oil saturation in sandstone cores by use of viscoelastic polymers. *SPE Journal*, *22*(2), 447–458. SPE-179689-PA. https://doi.org/10.2118/179689-PA

Reynolds, C. A., Menke, H., Andrew, M., Blunt, M. J., & Krevor, S. (2017). Dynamic fluid connectivity during steady-state multiphase flow in a sandstone. *Proceedings of the National Academy of Sciences*, *114*(31), 8187–8192. https://doi.org/10.1073/pnas.1702834114

Roof, J. G. (1970). Snap-off of oil droplets in water-wet pores. *SPE Journal*, *10*(01), 85–90. SPE-2504-PA. https://doi.org/10.2118/2504-PA

Sandengen, K., Kristoffersen, A., Melhuus, K., & Jøsang, L. O. (2016). Osmosis as mechanism for low-salinity enhanced oil recovery. *SPE Journal*, *21*(4), 1227–1235. SPE-179741-PA. https://doi.org/10.2118/179741-PA

Sandengen, K., Melhuus, K., & Kristoffersen, A. (2017). Polymer "Viscoelastic Effect"; does it reduce residual oil saturation. *Journal of Petroleum Science and Engineering*, *153*, 355–363. https://doi.org/10.1016/j.petrol.2017.03.029

Sheng, J. (2010). *Modern chemical enhanced oil recovery: Theory and practice*. Gulf Professional Publishing.

Soerens, T. S., Sabatini, D. A., & Harwell, J. H. (1998). Effects of flow bypassing and nonuniform NAPL distribution on the Nass Transfer Characteristics of NAPL dissolution. *Water Resources Research*, *34*(7), 1657–1673. https://doi.org/10.1029/98WR00554

Sohrabi, M., Mahzari, P., Farzaneh, S. A., Mills, J. R., Tsolis, P., & Ireland, S. (2017). Novel insights into mechanisms of oil recovery by use of low-salinity-water injection. *SPE Journal*, *22*(2), 407–416. SPE-172778-PA. https://doi.org/10.2118/172778-PA

Sorbie, K. S. (1991). *Polymer-improved oil recovery*. Springer.

Tanino, Y., & Christensen, M. (2019). Imbibition capillary pressure and relative permeability of mixed-wet microporous rock: New insights from history matching. *Transport in Porous Media*, *129*, 121–148. https://doi.org/10.1007/s11242-019-01280-4

Tetteh, J. T., Brady, P. V., & Ghahfarokhi, R. B. (2020). Review of low salinity waterflooding in carbonate rocks: Mechanisms, investigation techniques, and future directions. *Advances in Colloid and Interface Science*, *284*, 102253. https://doi.org/10.1016/j.cis.2020.102253

Vermolen, E. C. M., van Haasterecht, M. J. T., & Masalmeh, S. K. (2014). A systematic study of the polymer visco-elastic effect on residual oil saturation by core flooding. In *Presented at SPE EOR Conference at Oil and Gas West Asia, 31 March-2 April, Muscat, Oman*. SPE-169681-MS. https://doi.org/10.2118/169681-MS

Volpert, E., Selb, J., & Candau, F. (1998). Associating behavior of polyacrylamides hydrophobically modified with dihexylacrylamide. *Polymer*, *39*(5), 1025–1033. https://doi.org/10.1016/S0032-3861(97)00393-5

Wang, D., Cheng, J., Yang, Q., Gong, W., Li, Q., & Chen, F. (2000). Viscous-elastic polymer can increase microscale displacement efficiency in cores. In *Presented at SPE Annual Technical Conference and Exhibition, 1-4 October, Dallas, Texas*. SPE-63227-MS. https://doi.org/10.2118/63227-MS

Wang, D., Xia, H., Liu, Z., & Yang, Q. (2001). Study of the mechanism of polymer solution with visco-elastic behavior increasing microscopic oil displacement efficiency and the forming of steady "oil thread" flow channels. In *Presented at SPE Asia Pacific Oil and Gas Conference and Exhibition, 17-19 April, Jakarta, Indonesia*. SPE-68723-MS. https://doi.org/10.2118/68723-MS

Wang, S., Tokunaga, T. K., Wan, J., Dong, W., & Kim, Y. (2016). Capillary pressure-saturation relations in quartz and carbonate sands: Limitations for correlating capillary and wettability influences on air, oil, and supercritical CO_2 trapping. *Water Resources Research*, *52*(8), 6671–6690. https://doi.org/10.1002/2016WR018816

Wildenschild, D., & Sheppard, A. P. (2013). X-Ray imaging and analysis techniques for quantifying pore-scale structure and processes in subsurface porous medium systems. *Advances in Water Resources*, *51*, 217–246. https://doi.org/10.1016/j.advwatres.2012.07.018

Wu, T., & Firoozabadi, A. (2021). Surfactant-enhanced spontaneous emulsification near the crude oil-water interface. *Langmuir*, *37*(15), 4736–4743. https://doi.org/10.1021/acs.langmuir.1c00725

Xia, H., Wang, D., Wu, J., & Kong, F. (2004). Elasticity of HPAM solutions increases displacement efficiency under mixed wettability conditions. In *Presented at SPE Asia Pacific Oil and Gas Conference and Exhibition, 18-20 October, Perth, Australia*. SPE-88456-MS. https://doi.org/10.2118/88456-MS

Xia, H., Wang, D., Wu, W., & Jiang, H. (2007). Effect of the visco-elasticity of displacing fluids on the relationship of capillary number and displacement efficiency in weak oil-wet cores. In *Presented at Asia Pacific Oil and Gas Conference and Exhibition, 30 October-1 November, Jakarta, Indonesia*. SPE-109228-MS. https://doi.org/10.2118/109228-MS

Xie, C., Xu, K., Mohanty, K. K., Wang, M., & Balhoff, M. T. (2020). Nonwetting droplet oscillation and displacement by viscoelastic fluids. *Physical Review Fluids*, *5*, 063301. https://doi.org/10.1103/PhysRevFluids.5.063301

Xu, K., Liang, T., Zhu, P., Qi, P., Lu, J., Huh, C., & Balhoff, M. (2017). A 2.5-D glass micromodel for investigation of multiphase flow in porous media. *Lab on a Chip*, *17*(4), 640–646. https://doi.org/10.1039/c6lc01476c

Yun, W., Chang, S., Cogswell, D. A., Eichmann, S. L., Gizzatov, A., Thomas, G., et al. (2020). Toward reservoir-on-a-chip: Rapid performance evaluation of enhanced oil recovery surfactants for carbonate reservoirs using a calcite-coated micromodel. *Scientific Reports*, *10*, 782. https://doi.org/10.1038/s41598-020-57485-x

Zhong, L., Mayer, A., & Glass, R. J. (2001). Visualization of surfactant-enhanced nonaqueous phase liquid mobilization and solubilization in a two-dimensional micromodel. *Water Resources Research*, *37*(3), 523–537. https://doi.org/10.1029/2000WR900300

References From the Supporting Information

Varshney, A., & Steinberg, V. (2017). Elastic wake instabilities in a creeping flow between two obstacles. *Physical Review Fluids*, *2*(5), 051301. https://doi.org/10.1103/PhysRevFluids.2.051301

Walkama, D. M., Waisbord, N., & Guasto, J. S. (2020). Disorder suppresses chaos in viscoelastic flows. *Physical Review Letters*, *124*, 164501. https://doi.org/10.1103/PhysRevLett.124.164501